

Corrected Trapezoidal Rules for Near-Singular Surface Integrals Applied to 3D Interfacial Stokes Flow

Monika Nitsche^{a,*}, Bowei Wu^b, Ling Xu^c

^a*Department of Mathematics and Statistics, University of New Mexico, Albuquerque, 87108, NM, USA*

^b*Department of Mathematics and Statistics, University of Massachusetts Lowell, Lowell, 01854, MA, USA*

^c*Department of Mathematics and Statistics, North Carolina A & T State
University, Greensboro, 27411, NC, USA*

Abstract

Interfacial Stokes flow can be efficiently computed using the Boundary Integral Equation method. In 3D, the fluid velocity at a target point is given by a 2D surface integral over all interfaces, thus reducing the dimension of the problem. A core challenge is that for target points near, but not on, an interface, the surface integral is near-singular and standard quadratures lose accuracy. This paper presents a method to accurately compute the near-singular integrals arising in elliptic boundary value problems in 3D. It is based on a local series approximation of the integrand about a base point on the surface, obtained by orthogonal projection of the target point onto the surface. The elementary functions in the resulting series approximation can be integrated to high accuracy in a neighborhood of the base point using a recursive algorithm. The remaining integral is evaluated numerically using a standard quadrature rule, chosen here to be the 4th order Trapezoidal rule. The method is reduced to the standard quadrature plus a correction, and is uniformly of 4th order. The method is applied to resolve Stokes flow past several ellipsoidal rigid bodies. We compare the error in the velocity near the bodies, and in the time and displacement of particles traveling around the bodies, computed with and without the corrections.

Keywords: Stokes flow, boundary integral equation, near-singular quadrature

1. Introduction

The Stokes equation modeling highly viscous flow in the zero-inertia limit is an elliptic partial differential equation whose solution can be computed using the Boundary Integral Equation (BIE) method [13, 20]. The BIE approach is especially efficient for particulate fluid flows – viscous flows that contain soft or rigid bodies such as red blood cells, vesicles, drops, bubbles, colloidal particles, and micro swimmers – in which constraints placed on the interface between body interior and exterior enter the boundary integral representation of the fluid velocity. Accurate resolution of near fluid-particle or particle-particle interactions

*corresponding author email: nitsche@unm.edu

is essential for the accuracy of the overall numerical scheme and the stability of long-term simulations. A core challenge is the accurate evaluation of the Stokes boundary integral operators, also known as layer potentials, at target points close to, but not on, the boundary surface. These integrals are near-singular and notoriously difficult to approximate using standard quadrature rules.

Considerable research efforts have focused on developing efficient near-singular quadrature schemes for integral operators associated with elliptic PDEs. These quadrature methods can be loosely categorized into four classes. The first class of methods exploits the smoothness of layer potentials in the far-field. Klöckner et al. [12] introduced the QBX method, in which an accurate series expansion is constructed in the far field and then evaluated at target points near or on the boundary. Similarly, the piecewise surface quadratures of Ying et al. [27] and of Morse et al. [14] use interpolation or extrapolation of the far-field integral values to the near-field. A second class of methods is based on harmonic analysis. Helsing and Ojala [9] developed panel quadratures using complex interpolation to write near-singular line integrals as a series of integrals that can be evaluated analytically using recursion. Zhu and Veerapaneni [28] extended this method to triangulated surfaces using harmonic polynomial interpolation based on quaternion algebra. Perez-Arancibia et al. [19] used interpolation of the density function together with Green’s identities to regularize the integrand. The global quadrature of Barnett et al. [1] expresses the layer potentials as Cauchy integrals and evaluates them using a spectrally accurate barycentric formula derived from singularity subtraction. A third class of methods are the regularized quadratures of Beale and collaborators [2, 3] who compute regularized singular or near-singular integrands and then correct the regularization errors using asymptotic approximations. The method presented in this paper belongs to a fourth class: error corrections for regular quadratures applied to singular or near-singular integrals. Carvalho et al. [4, 11] find asymptotic error expansions for near-singular integrals on closed curves in 2D based on the periodic trapezoidal rule, and on 3D surfaces based on a local auxiliary polar mesh. Most other existing error correction methods are based on the trapezoidal rule and are for singular integrals [6, 25, 24, 10]. Wu [23] has recently generalized the Euler-Maclaurin formulas for singular integrals [21] to near-singular integrals, using a connection between polygamma functions and the Riemann zeta series. Closely related are the methods of Nitsche [15, 16], where the near-singular errors are obtained using local approximations of the integrand that can be integrated exactly. With this approach, corrected trapezoidal rules were obtained for planar vortex sheet flow and for axi-symmetric Stokes flow. They were recently applied to compute the motion of interacting flapping plates [17] and of freely falling plates [22].

This paper generalizes the latter approach to evaluate surface integrals in 3D of the form

$$\int_S \frac{F(\mathbf{x}, \mathbf{x}_0)}{|\mathbf{x} - \mathbf{x}_0|^r} \omega(\mathbf{x}) dS, \quad (1.1)$$

for odd integers $r = 1, 3, 5, \dots$ that occur in the BIE approach for elliptic problems. These integrals are near-singular when the target point \mathbf{x}_0 is near, but not on, S . They are integrable in the principal value sense when \mathbf{x}_0 is on S . The method consists of using Taylor series to find local approximations of the integrand about the orthogonal projection of the

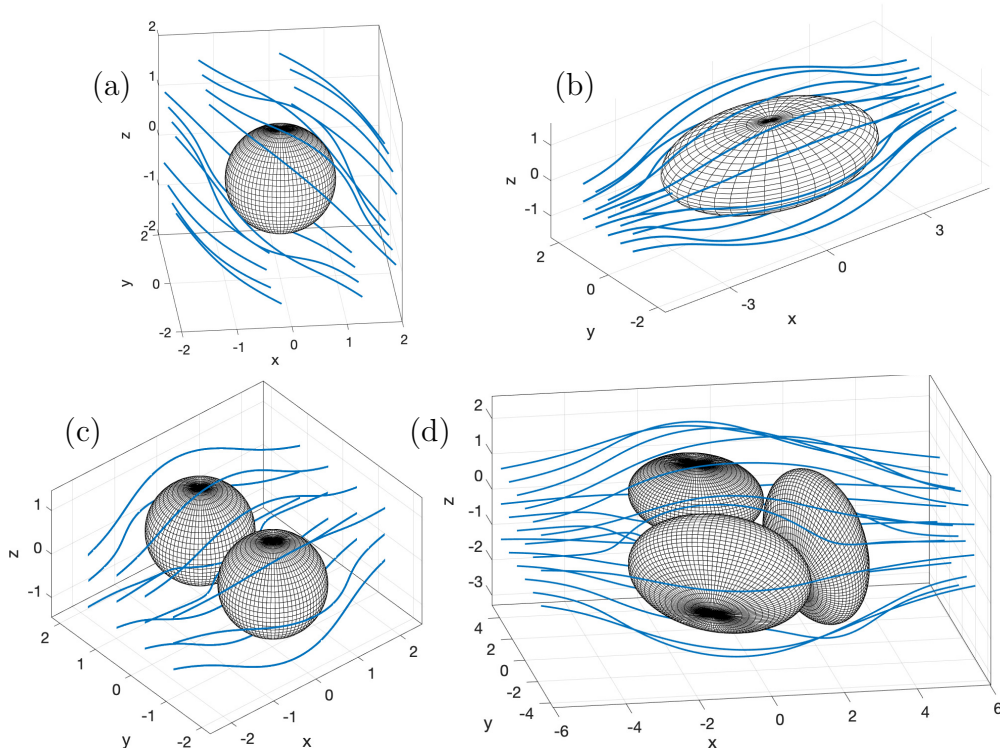


Figure 1: Stokes flow (a) past sphere, (b) past ellipsoid, (c) past two spheres, (d) past three ellipsoids.

target point onto the surface. The basis functions in the resulting expansion capture the near-singularity of the integrand and are integrated to high accuracy in a neighbourhood of the projection. The remaining integral is computed using a standard quadrature, chosen here to be a 4th order trapezoidal rule. The number of terms kept in the Taylor approximation of the integrand is determined using upper bounds on the trapezoidal errors of their integrals. The result reduces to the standard trapezoidal rule plus a correction, and is uniformly of 4th order. The method is applied to resolve Stokes flow past several ellipsoidal rigid bodies, for the four examples illustrated in Fig. 1. We confirm 4th order convergence in the fluid velocity near the bodies, and determine the effect of the corrections on the time and displacement of particles traveling around the bodies.

As mentioned, the method introduced here generalizes that for line integrals introduced in [15]. In that case, the basis functions of the local approximations can be integrated exactly. In the present case of surface integrals, the basis functions do not have readily available antiderivatives. Inspired by the recurrence relations for singular integrals in Helsing [8], we derive a recurrence relation for a family of near-singular integrals that returns highly accurate integral values. Details of the derivation will be presented in forthcoming work.

The paper is organized as follows. Section 2 formulates the fluid velocity in terms of single and double layer potentials. Section 3 presents the numerical method, including the local approximation, the recurrence relation used to integrate the basis function, and details of the implementation. Section 4 presents numerical results for the four sample Stokes flows. A summary is presented in Section 5.

2. Stokes Flow Past Objects

Consider Stokes flow past a body with surface S , driven by a far-field flow \mathbf{u}_∞ . The velocity at a *target point* \mathbf{x}_0 is given in terms of the single and double layer potentials (SLP and DLP),

$$\mathbf{u}(\mathbf{x}_0) = \mathbf{u}_\infty + \mathcal{S}[\mathbf{f}](\mathbf{x}_0) + \mathcal{D}[\mathbf{f}](\mathbf{x}_0), \quad (2.1)$$

where

$$\mathcal{S}[\mathbf{f}](\mathbf{x}_0) = \frac{1}{8\pi\mu} \int_S \left(\frac{\mathbf{f}}{\rho} + \frac{(\mathbf{f} \cdot \widehat{\mathbf{x}}) \widehat{\mathbf{x}}}{\rho^3} \right) dS(\mathbf{x}), \quad (2.2a)$$

$$\mathcal{D}[\mathbf{f}](\mathbf{x}_0) = -\frac{3}{4\pi} \int_S \frac{(\mathbf{f} \cdot \widehat{\mathbf{x}}) \widehat{\mathbf{x}} (\widehat{\mathbf{x}} \cdot \mathbf{n})}{\rho^5} dS(\mathbf{x}) \quad (2.2b)$$

Here $\rho^2 = |\mathbf{x} - \mathbf{x}_0|^2$ and $\widehat{\mathbf{x}} = \mathbf{x} - \mathbf{x}_0$ [20, Eq 2.3.11]. That is, the integrals are of the form (1.1) with $r = 1, 3, 5$, and are near-singular if \mathbf{x}_0 is near S . For flow past several objects E_k , $k = 1, \dots, N$, such as illustrated in Fig. 1(c,d), the velocity is

$$\mathbf{u}(\mathbf{x}_0) = \mathbf{u}_\infty + \sum_{k=1}^N \left(\mathcal{S}_k[\mathbf{f}_k](\mathbf{x}_0) + \mathcal{D}_k[\mathbf{f}_k](\mathbf{x}_0) \right) \quad (2.3)$$

and \mathcal{S}_k and \mathcal{D}_k are the Stokes SLP and DLP on the object E_k . In all our examples below, the far field \mathbf{u}_∞ is constant and the body velocity is zero.

The functions \mathbf{f}_k are referred to as the density on body E_k . They are determined by the no-slip boundary condition: the fluid velocity equals the body velocity on all S_k . For zero body velocity,

$$\mathbf{u}(\mathbf{x}) = \mathbf{0} \text{ for all } \mathbf{x} \in S_k, \quad k = 1, \dots, N. \quad (2.4)$$

For flow past a sphere, the density is known analytically to be $\mathbf{f} = -1.5\mathbf{u}_\infty$ [18]. In all other cases, \mathbf{f}_k is obtained numerically as follows. Each S_k is discretized by a set \mathbf{X}_k of $n_k \times m_k$ grid points. The integrals \mathcal{S} and \mathcal{D} are discretized using the grid point function values. Then (2.4) reduces to a linear system of $N \times N$ blocks of size $n_k m_k \times n_k m_k$, $k = 1, \dots, N$, for the unknowns \mathbf{f}_k ,

$$\frac{1}{2}\mathbf{f}_k + \sum_{k'=1}^N \mathbf{A}_{kk'} \mathbf{f}_{k'} = -\mathbf{u}_\infty, \quad k = 1, \dots, N, \quad (2.5a)$$

where

$$\mathbf{A}_{kk'} \mathbf{f}_{k'} = \mathcal{S}_{k'}[\mathbf{f}_{k'}](\mathbf{x}_j) + \mathcal{D}_{k'}[\mathbf{f}_{k'}](\mathbf{x}_j), \quad \mathbf{x}_j \in X_k. \quad (2.5b)$$

This system is solved by GMRES iteration.

The term $\frac{1}{2}\mathbf{f}_k$ in (2.5a) accounts for the jump condition in the double layer when \mathbf{x}_j lies on \mathbf{X}_k [20, Eq 2.1.12]. The diagonal entries $\mathbf{A}_{kk}\mathbf{f}_k$ describe the self-induced velocity of the body E_k at a point \mathbf{x}_j on itself. The corresponding singular integrals are evaluated using spectral quadrature with a fast grid rotation algorithm [7]. The off-diagonal entries $\mathbf{A}_{kk'}\mathbf{f}_{k'}$, $k \neq k'$, describe the velocity induced by $S_{k'}$ at points on S_k . If the body E_k is sufficiently close to $E_{k'}$, the corresponding integrals are nearly singular for nearby points $\mathbf{x}_j \in \mathbf{X}_k$. These are evaluated using the method described below.

3. Numerical Method

3.1. Basic Overview

Consider an integral of form (1.1) over a body E with boundary surface S . We assume that S is *logically rectangular*, that is, it can be parametrized by $\mathbf{x}(\alpha, \beta)$ where (α, β) range over a rectangle D . After the change of variables, the integral over D is approximated by a quadrature T_D , chosen here to be a high-order trapezoidal rule,

$$\int_D \frac{F(\mathbf{x}(\alpha, \beta), \mathbf{x}_0)}{\rho^r} \omega(\mathbf{x}(\alpha, \beta)) J(\alpha, \beta) d\alpha d\beta = \int_D G(\alpha, \beta) d\alpha d\beta \approx T_D[G]. \quad (3.1)$$

Here $J = |\mathbf{x}_\alpha \times \mathbf{x}_\beta|$, G denotes the integrand, and the subscript on T_D denotes the domain of integration.

If the target point \mathbf{x}_0 is far from the surface S , the chosen trapezoidal rule yields uniformly high accuracy. If the target point is so close that the integral is near singular, the trapezoidal rule loses accuracy. In that case, we find a local approximation H of G that (1) captures the near-singularity and (2) can essentially be integrated exactly over a subdomain (or window) W of D . The smoother function $G - H$ is then integrated numerically over W , while G is integrated numerically over the remaining domain. This is summarized as

$$\begin{aligned} \int_D G &= \int_{D \setminus W} G + \int_W (G - H) + \int_W H \\ &\approx T_{D \setminus W}[G] + T_W[G - H] + \int_W H \\ &= T_D[G] + E_W[H], \end{aligned} \quad (3.2)$$

where

$$E_W[H] = \int_W H - T_W[H]. \quad (3.3)$$

That is, it amounts to simply computing the trapezoid approximation $T_D[G]$ and adding a correction $E_W[H]$. The window W is an approximately square subgrid of D . For $T_D[G]$ we use a 4th order trapezoidal rule (given in §3.5). For reasons explained in §3.6, we use a higher 6th order approximation for $T_W[H]$. The final results are uniformly 4th order accurate over all target points \mathbf{x}_0 .

The approximation H is obtained by expanding G about the base point (α_b, β_b) determined by the orthogonal projection of \mathbf{x}_0 onto S , using Taylor series. The resulting expansion

$$G(\alpha, \beta) \approx H(\alpha, \beta) = \sum c_{pqk} H_{pqk}(\alpha - \alpha_b, \beta - \beta_b), \quad (3.4a)$$

is given in terms of basis functions

$$H_{pqk}(\alpha, \beta) = \frac{\alpha^p \beta^q}{\rho_o^{2k+1}}, \quad \rho_o^2 = d^2 + c_\alpha^2 \alpha^2 + 2c_{\alpha\beta} \alpha\beta + c_\beta^2 \beta^2. \quad (3.4b)$$

These functions capture the near-singular behaviour of G . Moreover, while analytic expressions for their antiderivatives are not readily available, a recursion for $\int_W H_{pqk}$ enables quick and accurate integration. All necessary details are given next.

3.2. Parametrization and discretization

Standard ellipsoid. For simplicity, all objects considered here are ellipsoids. Consider first a single ellipsoid E centered at the origin of a Cartesian coordinate system, with major axes aligned with the coordinate axes, and surface S given by

$$\frac{x^2}{a^2} + \frac{y^2}{b^2} + \frac{z^2}{c^2} = 1. \quad (3.5)$$

This is referred to as a *standard ellipsoid*. The surface is parametrized by latitude-longitude coordinates $\alpha \in [-\pi, \pi]$ and $\beta \in [-\pi/2, \pi/2]$, and is discretized by $n \times m$ points $\mathbf{x}(\alpha_j, \beta_k)$, where $\alpha_j = -\pi + 2\pi j/n, \beta_k = -\pi/2 + \pi k/m, j = 0, \dots, n, k = 0, \dots, m$. However, the trapezoid rule loses accuracy for target points near the poles of such a latitude-longitude grid. We thus use two different grids, one with the poles on the z -axis, a second with poles on the x -axis. For a given target point \mathbf{x}_0 , we choose the grid whose poles are furthest from \mathbf{x}_0 . The two grids are given by

$$\mathbf{x} = \langle a \cos \alpha \cos \beta, b \sin \alpha \cos \beta, c \sin \beta \rangle \quad (\text{Grid 1}) \quad (3.6a)$$

$$\mathbf{x} = \langle a \sin \beta, b \cos \alpha \cos \beta, c \sin \alpha \cos \beta \rangle \quad (\text{Grid 2}) \quad (3.6b)$$

Grid 1 has poles at $(0, 0, \pm c)$, and is discretized by $n = n_1, m = m_1$ points. Grid 2 has poles at $(\pm a, 0, 0)$, and is discretized by $n = n_2, m = m_2$ points. They are shown in Fig. 2 for a sample ellipsoid, sample target point \mathbf{x}_0 , and sample values of n_1, m_1, n_2, m_2 .

Computing the SLP and DLP using (3.1) requires J (for SLP) and nJ (for DLP). For both parametrizations (3.6a,b), they are given by

$$nJ = \mathbf{x}_\alpha \times \mathbf{x}_\beta = abc \cos \beta \left\langle \frac{x}{a^2}, \frac{y}{b^2}, \frac{z}{c^2} \right\rangle \quad (3.7a)$$

$$J = |\mathbf{x}_\alpha \times \mathbf{x}_\beta| = abc \cos \beta \sqrt{\frac{x^2}{a^4} + \frac{y^2}{b^4} + \frac{z^2}{c^4}}. \quad (3.7b)$$

Standardization of general ellipsoid. In general, and in all our multi-ellipsoid examples, each ellipsoid $E_k, k = 1, \dots, N$, is not in standard form, but is given as a rotation and translation of a standard ellipsoid \tilde{E}_k with

$$E_k = \mathbf{R}_k \tilde{E}_k + \mathbf{s}_k, \quad k = 1, \dots, N$$

where \mathbf{s}_k is a translation vector, and $\mathbf{R}_k := \mathbf{BCD}$ is a rotation matrix, with

$$\mathbf{B} = \begin{bmatrix} \cos \phi_k & -\sin \phi_k & 0 \\ \sin \phi_k & \cos \phi_k & 0 \\ 0 & 0 & 1 \end{bmatrix}, \quad \mathbf{C} = \begin{bmatrix} 1 & 0 & 0 \\ 0 & \cos \theta_k & -\sin \theta_k \\ 0 & \sin \theta_k & \cos \theta_k \end{bmatrix}, \quad \mathbf{D} = \begin{bmatrix} \cos \psi_k & -\sin \psi_k & 0 \\ \sin \psi_k & \cos \psi_k & 0 \\ 0 & 0 & 1 \end{bmatrix}.$$

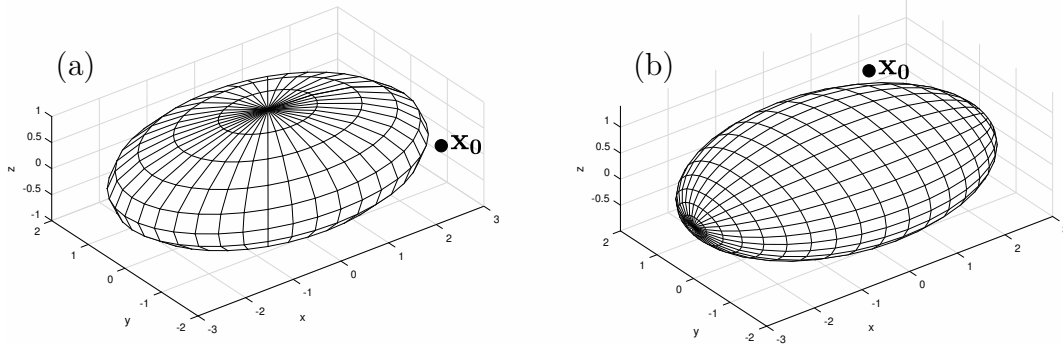


Figure 2: Sample set of two grids for a standard ellipsoid with $a = 3$, $b = 2$, $c = 1$, and sample target point \mathbf{x}_0 . (a) Grid 1, with $n_1 = 10$, $m_1 = 40$, poles on z -axis. (b) Grid 2, with $n_2 = 20$, $m_2 = 30$, poles on x -axis. For given \mathbf{x}_0 , choose the grid whose poles are furthest from \mathbf{x}_0 .

We use rotation and translation to reduce the computation of the SLP and DLP over non-standard ellipsoids to that over the corresponding standard ellipsoid: letting

$$\mathbf{x} = \mathbf{R}_k \tilde{\mathbf{x}} + \mathbf{s}_k, \quad \mathbf{x}_0 = \mathbf{R}_k \tilde{\mathbf{x}}_0 + \mathbf{s}_k, \quad \mathbf{f}_k = \mathbf{R}_k \tilde{\mathbf{f}}_k$$

we have that

$$\begin{aligned} \mathcal{S}_k[\mathbf{f}_k](\mathbf{x}_0) &= \frac{1}{8\pi\mu} \int_{S_k} \left(\frac{\mathbf{f}_k}{\rho} + \frac{(\mathbf{f}_k \cdot \hat{\mathbf{x}}) \hat{\mathbf{x}}}{\rho^3} \right) dS(\mathbf{x}), \\ &= \frac{1}{8\pi\mu} \int_{\tilde{S}_k} \left(\frac{\mathbf{R}_k \tilde{\mathbf{f}}_k}{\tilde{\rho}} + \frac{(\mathbf{R}_k \tilde{\mathbf{f}}_k \cdot \mathbf{R}_k \hat{\tilde{\mathbf{x}}}) \mathbf{R}_k \hat{\tilde{\mathbf{x}}}}{\tilde{\rho}^3} \right) dS(\tilde{\mathbf{x}}), \\ &= \frac{1}{8\pi\mu} \mathbf{R}_k \int_{\tilde{S}_k} \left(\frac{\tilde{\mathbf{f}}_k}{\tilde{\rho}} + \frac{(\tilde{\mathbf{f}}_k \cdot \hat{\tilde{\mathbf{x}}}) \hat{\tilde{\mathbf{x}}}}{\tilde{\rho}^3} \right) dS(\tilde{\mathbf{x}}), \\ &= \mathbf{R}_k \mathcal{S}_{\tilde{k}}[\tilde{\mathbf{f}}_k](\tilde{\mathbf{x}}_0), \end{aligned} \tag{3.8}$$

where $\hat{\tilde{\mathbf{x}}} = \tilde{\mathbf{x}} - \tilde{\mathbf{x}}_0$, $\tilde{\rho} = |\tilde{\mathbf{x}} - \tilde{\mathbf{x}}_0|$, \tilde{S}_k is the rotated surface, and we used that $\mathbf{R}_k \hat{\tilde{\mathbf{x}}} = \hat{\tilde{\mathbf{x}}}$, $\tilde{\rho} = \rho$, $dS(\mathbf{x}) = dS(\tilde{\mathbf{x}})$, and $\mathbf{R}_k \tilde{\mathbf{f}}_k \cdot \mathbf{R}_k \hat{\tilde{\mathbf{x}}} = \tilde{\mathbf{f}}_k \cdot \hat{\tilde{\mathbf{x}}}$ since \mathbf{R}_k is orthogonal. Similarly, $\mathcal{D}_k[\mathbf{f}_k](\mathbf{x}_0) = \mathbf{R}_k \mathcal{D}_{\tilde{k}}[\tilde{\mathbf{f}}_k](\tilde{\mathbf{x}}_0)$.

3.3. The approximation H

We wish to approximate the integrand in (3.1),

$$G(\alpha, \beta) = \frac{F(\mathbf{x}(\alpha, \beta), \mathbf{x}_0)}{\rho^r} \omega(\mathbf{x}(\alpha, \beta)) J(\alpha, \beta), \tag{3.9}$$

where F, ω, J are smooth and $\rho = |\mathbf{x}(\alpha, \beta) - \mathbf{x}_0|$, by a function $H(\alpha, \beta)$ that captures the near-singularity and can be integrated exactly in closed form. The approximation H is

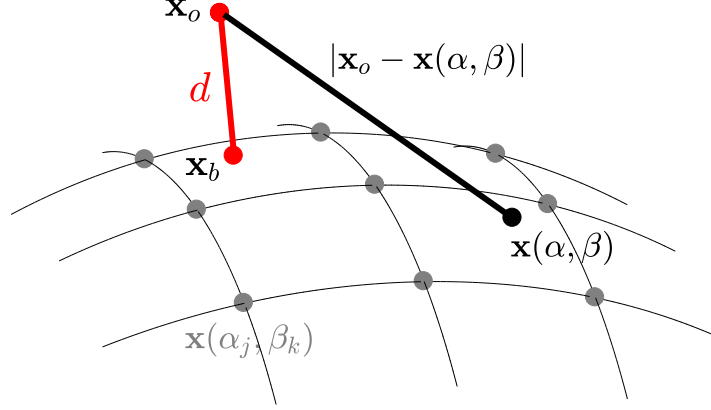


Figure 3: Sketch showing surface $\mathbf{x}(\alpha, \beta)$, discretization by $\mathbf{x}(\alpha_j, \beta_k)$, target point \mathbf{x}_0 , and corresponding distance d and base point \mathbf{x}_b .

obtained by expanding $G(\alpha, \beta)$ about a base point (α_b, β_b) , defined by $\mathbf{x}_b = \mathbf{x}(\alpha_b, \beta_b)$, where \mathbf{x}_b is the orthogonal projection of \mathbf{x}_0 onto S , as illustrated in Fig. 3.

We begin by expanding $\mathbf{x}(\alpha, \beta)$ about the base point,

$$\mathbf{x} = \mathbf{x}_b + \mathbf{x}_\alpha \hat{\alpha} + \mathbf{x}_\beta \hat{\beta} + \frac{\mathbf{x}_{\alpha\alpha}}{2} \hat{\alpha}^2 + \mathbf{x}_{\alpha\beta} \hat{\alpha} \hat{\beta} + \frac{\mathbf{x}_{\beta\beta}}{2} \hat{\beta}^2 + \frac{\mathbf{x}_{\alpha\alpha\alpha}}{6} \hat{\alpha}^3 + \frac{\mathbf{x}_{\alpha\alpha\beta}}{2} \hat{\alpha}^2 \hat{\beta} + \dots \quad (3.10)$$

where $\hat{\alpha} = \alpha - \alpha_b$, $\hat{\beta} = \beta - \beta_b$. In view of the orthogonality properties $(\mathbf{x}_b - \mathbf{x}_0) \perp \mathbf{x}_\alpha$ and $(\mathbf{x}_b - \mathbf{x}_0) \perp \mathbf{x}_\beta$, we obtain the Taylor expansion of ρ^2 ,

$$\rho^2 = |\mathbf{x} - \mathbf{x}_0|^2 = d^2 + c_\alpha^2 \hat{\alpha}^2 + 2c_{\alpha\beta} \hat{\alpha} \hat{\beta} + c_\beta^2 \hat{\beta}^2 + \eta(\hat{\alpha}, \hat{\beta}) = \rho_0^2 \left[1 + \frac{\eta}{\rho_0^2} \right] \quad (3.11)$$

where

$$\rho_0^2 = d^2 + c_\alpha^2 \hat{\alpha}^2 + 2c_{\alpha\beta} \hat{\alpha} \hat{\beta} + c_\beta^2 \hat{\beta}^2, \quad (3.12)$$

and

$$\begin{aligned} d &= |\mathbf{x}_b - \mathbf{x}_0|, \\ c_\alpha^2 &= (\mathbf{x}_b - \mathbf{x}_0) \cdot \mathbf{x}_{\alpha\alpha} + \mathbf{x}_\alpha \cdot \mathbf{x}_\alpha, \\ c_{\alpha\beta} &= (\mathbf{x}_b - \mathbf{x}_0) \cdot \mathbf{x}_{\alpha\beta} + \mathbf{x}_\alpha \cdot \mathbf{x}_\beta, \\ c_\beta^2 &= (\mathbf{x}_b - \mathbf{x}_0) \cdot \mathbf{x}_{\beta\beta} + \mathbf{x}_\beta \cdot \mathbf{x}_\beta, \end{aligned} \quad (3.13)$$

with all derivatives evaluated at the base point, and where $\eta = \sum_{j+k=3}^{\infty} e_{jk} \hat{\alpha}^j \hat{\beta}^k$ is the degree 3 and higher terms in the expansion of ρ^2 . We then expand F/ρ^r with respect to η/ρ_0^2 as

$$\frac{F}{\rho^r} = \frac{F}{\rho_0^r} \left[1 - \frac{r}{2} \frac{\eta}{\rho_0^2} + \frac{r(r+2)}{8} \frac{\eta^2}{\rho_0^4} - \frac{r(r+2)(r+4)}{48} \frac{\eta^3}{\rho_0^6} + \dots \right] \quad (3.14)$$

and $F = \sum_{j+k=0}^{\infty} \tilde{c}_{jk} \hat{\alpha}^j \hat{\beta}^k$. With additional multiplication by Taylor series approximations of $\omega(\alpha, \beta)J(\alpha, \beta)$ and odd values of r we obtain the expansion of G in the form

$$G(\alpha, \beta) \approx H(\alpha, \beta) = \sum c_{pqk} H_{pqk}(\hat{\alpha}, \hat{\beta}), \quad (3.15a)$$

where

$$H_{pqk}(\alpha, \beta) = \frac{\alpha^p \beta^q}{\rho_o^{2k+1}}. \quad (3.15b)$$

H consists of a truncation of the expansion (3.14). The number of terms that are kept in the expansion of H in (3.15) are determined using the known bound for the trapezoidal rule error due to the near-singular behavior of each basis functions [15],

$$E[H_{pqk}] = O(h^2 d^{p+q-(2k+1)}). \quad (3.16)$$

We keep all terms in $E[H]$ that are bigger than $O(h^4)$, where $h = \max(\hat{\alpha}, \hat{\beta}, d)$. That is, we keep all terms with $2 + p + q - (2k + 1) \leq 3$, or $p + q \leq (2k + 1) + 1$.

The size of F affects the number of terms needed in the expansion, and the accuracy needed for the density ω . To illustrate, note that for the Stokes SLP, the term with $r = 1$ has corresponding $F = O(1)$, while the term with $r = 3$ has corresponding $F = O(d^2)$. For the DLP, the term with $r = 5$ has $F = O(d^3)$. So the integrand has the form

$$G = \frac{F\omega}{\rho_o^r} \left(1 + \frac{O(\eta)}{\rho_o^2} + \frac{O(\eta^2)}{\rho_o^4} + \dots \right) \quad (3.17)$$

where $F = O(d^m)$, some m , and $\eta = O(d^3)$. The n th term satisfies

$$E\left[\frac{F\omega\eta^n}{\rho_o^{r+2n}}\right] = O(h^2 d^{m+3n-(r+2n)}) = O(h^2 d^{m-r+n}). \quad (3.18)$$

So for 4th order, we need all $n \geq 0$ up to $2 + (m - r + n) < 4$, or

$$0 \leq n \leq r + 1 - m. \quad (3.19)$$

In terms of the needed basis functions, note that for each n , $\frac{F\omega\eta^n}{\rho_o^{r+2n}}$ contains $H_{pqk} = \frac{\alpha^p \beta^q}{\rho_o^{2k+1}}$ for $2k+1 = r+2n$ and $p+q \geq 3n$, for 4th order, by (3.16), we need H_{pqk} for all combinations of p, q up to $p+q - (2k+1) + 2 < 4$, or

$$3n \leq p+q \leq (2k+1) + 1 \equiv 2n + r + 1. \quad (3.20)$$

It follows, for example for $r = 1, m = 0$, that we need $n \leq 2$ with

$$\begin{aligned} n = 0 : & 0 \leq p+q \leq 2 \\ n = 1 : & 3 \leq p+q \leq 4 \\ n = 2 : & 6 \leq p+q \leq 6 \end{aligned} \quad (3.21)$$

so $F\omega$ is only needed to 2nd order. Repeating this exercise for $r = 3, m = 2$ and $r = 5, m = 3$, one finds that for 4th order, for both SLP and DLP, and $2k+1 = 1, 3, 5, 7, 9, 11$, respectively, we need $p+q = 0:2, 0:4, 0:6, 3:8, 6:10, 9:12$ which gives a total of 179 basis functions. In addition, \mathbf{x} is needed to 4th order, and the density ω is needed to third order.

From (3.17,3.18) one can also deduce the size of the errors in the uncorrected trapezoidal rule. They are given by the term in the expansion (3.17) with largest error, which corresponds to $n = 0$. It follows that the uncorrected trapezoidal rule is $O(h^2/d)$ for the SLP and $O(h^2/d^2)$ for the DLP.

Finally, we note that the expansion (3.14) requires that $\rho_0^2 > 0$ in (3.12) for any $d > 0$, and all α, β , which in turn requires that the quadratic form $c_\alpha^2 \hat{\alpha}^2 + 2c_{\alpha\beta} \hat{\alpha} \hat{\beta} + c_\beta^2 \hat{\beta}^2$ be positive definite (or equivalently, $c_\alpha^2 > 0$, $c_\beta^2 > 0$ and $0 \leq c_{\alpha\beta}^2 < c_\alpha^2 c_\beta^2$). This holds true provided either that the target point \mathbf{x}_0 is outside the ellipsoid, or that \mathbf{x}_0 is inside the ellipsoid within the radius of the osculating sphere at the base point, see Appendix B.

3.4. Recursive evaluation of $\int H_{pqk}$

To compute the corrections $E_W[H]$, we need to accurately and efficiently compute the integrals $\int H_{pqk}$ over a square subdomain W of the original domain approximately centered at (α_b, β_b) . With proper substitution, these integrals reduce to the form

$$\int_a^b \int_c^d \frac{u^p v^q}{\rho_u^{2k+1}} du dv, \quad \rho_u^2 = 1 + u^2 + 2Cuv + v^2, \quad (3.22)$$

where the domain is rectangular, approximately centered at the origin ($a \approx -b$, $d \approx -c$), and $|C| = \left| \frac{c_{\alpha\beta}}{c_\alpha c_\beta} \right| < 1$. For $C = 0$, analytical expressions for all antiderivatives can be found with Mathematica. However, for $C \neq 0$, such expressions are not readily available. Instead, we obtain all antiderivatives using the recursive algorithm presented next. The values of the definite integrals are computed from the antiderivatives at each step. The recursion, whose derivation will be presented in detail in an upcoming work, is similar to that given in [8] for the singular integrals obtained when $d = 0$.

Define the antiderivatives

$$I_{pqk} = \int \int \frac{u^p v^q}{\rho_u^{2k+1}} du dv,$$

for $|C| < 1$ and the required values $0 \leq p, q \leq 12$, and $0 \leq k \leq 5$. In a preparatory step, evaluate all one-dimensional integrals

$$F_{pk} = \int \frac{u^p}{\rho_u^{2k+1}} du, \quad G_{qk} = \int \frac{v^q}{\rho_u^{2k+1}} dv, \quad (3.23)$$

using the recursion given in Appendix A, starting with known analytic expressions for F_{00} and G_{00} . The values of I_{pqk} are then obtained as follows:

Step 0: Initialization. The definite integral of I_{005} is evaluated numerically. Here we use its exact value integrated over all of \mathbb{R}^2 , and approximate the difference between a sufficiently large domain and the actual rectangular domain using Gauss integration.

Step 1: Evaluate I_{00k} , all $k < 5$, using

$$I_{00k} = \frac{(2k+1)I_{00(k+1)} - uG_{0k} - vF_{0k}}{2k-1}, \quad k = 4 : -1 : 0. \quad (3.24)$$

These are computed backwards in k since the integrals, of magnitude $1/R^{2k-1}$, $R \approx \max(|a|, |c|)$, increases as k decreases, yielding a stable method. The reverse recursion, starting with I_{000} , is numerically unstable due to subtraction of like numbers.

Step 2: Evaluate I_{pqk} for all cases with $2k - p - q - 1 = 0$. Here we first use (3.25b) for $p = 0$, $q = 2k - p - 1$, all k , followed by (3.25a) for $q \geq 0$, $p = 2k - q - 1$, all k .

$$I_{pq(k+1)} = \frac{(n-1)I_{p(q-2)k} - cpI_{(p-1)(q-1)k} + cu^p G_{(q-1)k} - v^{q-1} F_{pk}}{(2k+1)(1-c^2)}, \quad (3.25a)$$

$$I_{pq(k+1)} = \frac{(p-1)I_{(p-2)qk} - cqI_{(p-1)(q-1)k} + cv^q F_{(p-1)k} - u^{p-1} G_{qk}}{(2k+1)(1-c^2)}, \quad (3.25b)$$

The terms with negative indices, for example in (3.25b) when $p = 1$ or $q = 0$, are not present since they are multiplied by 0. We note that all values of I_{pqk} on both sides of the recursion formulas are of approximately equal magnitude $\sim 1/R^2$, so there is no loss of accuracy due to subtraction of like numbers.

Step 3: Evaluate I_{pqk} for all cases with $2k - p - q - 1 \neq 0$. Here we first use (3.26b) for $q = 0$, $p \geq 1$ all k , followed by (3.26a) for $p \geq 0$, $q \geq 1$, all k .

$$I_{pqk} = \left[(q-1)I_{p(q-2)k} - cpI_{(p-1)(q-1)k} + cu^p G_{(q-1)k} - (1-c^2)u^{p+1}G_{qk} - (v^{q-1} + (1-c^2)v^{q+1})F_{pk} \right] / \left[(1-c^2)(2k-p-q-1) \right] \quad (3.26a)$$

$$I_{pqk} = \left[(p-1)I_{(p-2)qk} - cqI_{(p-1)(q-1)k} + cv^q F_{(p-1)k} - (1-c^2)v^{q+1}F_{pk} - (u^{p-1} + (1-c^2)u^{p+1})G_{qk} \right] / \left[(1-c^2)(2k-p-q-1) \right] \quad (3.26b)$$

where, as above, all I_{pqk} with negative indices are set to zero.

3.5. Trapezoidal Rules T^4 and T^6

The trapezoidal rules of fourth and sixth order used here to compute double integrals over rectangular domains discretized by a uniform mesh are obtained by applying the Euler-Maclaurin expansion for 1D integrals in each direction. We have that

$$\begin{aligned} \int_c^d \int_a^b f(\alpha, \beta) d\alpha d\beta &\approx \Delta\beta\Delta\alpha \sum_{k=0}^m \sum_{j=0}^n f(\alpha_j, \beta_k) \\ &- \frac{\Delta\beta\Delta\alpha^2}{12} \sum_{k=0}^m \left. \frac{\partial f}{\partial \alpha}(\alpha, \beta_k) \right|_{\alpha=a}^{\alpha=b} - \frac{\Delta\beta^2\Delta\alpha}{12} \sum_{j=0}^n \left. \frac{\partial f}{\partial \beta}(\alpha_j, \beta) \right|_{\beta=c}^{\beta=d} \\ &+ \frac{\Delta\beta\Delta\alpha^4}{720} \sum_{k=0}^m \left. \frac{\partial^3 f}{\partial \alpha^3}(\alpha, \beta_k) \right|_{\alpha=a}^{\alpha=b} + \frac{\Delta\beta^4\Delta\alpha}{720} \sum_{j=0}^n \left. \frac{\partial^3 f}{\partial \beta^3}(\alpha_j, \beta) \right|_{\beta=c}^{\beta=d} \\ &+ \frac{\Delta\beta^2\Delta\alpha^2}{12^2} \left. \frac{\partial^2 f}{\partial \alpha \partial \beta}(\alpha, \beta) \right|_{\alpha=a}^{\alpha=b} \Big|_{\beta=c}^{\beta=d} \end{aligned} \quad (3.27)$$

where the prime denotes that the first and last term in the sum are weighted by $1/2$. The first term on the right hand side is of order 1. The second and third are of order h^2 , where $h = \max \Delta\alpha, \Delta\beta$. The last three are all the terms in the expansion of order h^4 . The 2nd, 4th, and 6th order trapezoidal rules $T_D^2[f], T_D^4[f], T_D^6[f]$ are thus given by the first one, three and six terms on the right hand side, respectively. As described next, the method presented in this paper uses T^4 and T^6 . For ease of notation, function values at the (j, k) th grid point will be denoted below by indices j, k , for example, $f(\alpha_j, \beta_k) = f_{j,k}$.

3.6. On the size n_w of the window S

The method consists of correcting the trapezoidal approximation of near-singular integrals by integrating a local approximation exactly over a subdomain W centered on the near-singularity. Specifically, the approximation (3.2, 3.3), repeated here for clarity, is

$$\begin{aligned} \int_D G &= \int_{D \setminus W} G + \int_W (G - H) + \int_W H \\ &\approx T_{D \setminus W}[G] + T_W[G - H] + \int_W H \\ &= T_D[G] + E_W[H] \end{aligned} \tag{3.28}$$

Note that the term $T_W[G - H]$ requires sampling both G and H at the same grid points. The subdomain $W \subset D$ is thus chosen to be an $2n_w \times 2n_w$ subgrid of the original grid, roughly centered on (α_b, β_b) , $W = [\alpha_{j_0 - n_w}, \alpha_{j_0 + n_w}] \times [\beta_{k_0 - n_w}, \beta_{k_0 + n_w}]$ such that $(\alpha_{j_0}, \beta_{k_0})$ is the nearest grid point to (α_b, β_b) . Since W is rectangular, $\int_W H$ can easily be evaluated using the recursive formulas given above.

Next we describe how to choose the size of the window W . The term $E_W[H]$ captures the error of the trapezoidal approximation of near-singular integrals. This term is bounded by (3.16). However, it also contains the trapezoidal error due to derivatives at the boundary ∂W of W . If the window size $n_w h$ is small, the derivatives of H_{pqk} are large on ∂W . The size of these errors is best captured by the error in integrating H over the complement, $E_{D \setminus W}[H]$. This error is dominated by the boundary derivatives, since H is regular (and not near-singular) outside W . Furthermore, the error depends on the quadrature rule used.

Figure 4 plots the error in integrating a sample basis function, $H_{000}(x, y) = 1/\sqrt{x^2 + y^2 + d^2}$, $d = 0.001$, over the complement $D \setminus W$ of a window $W = [-n_w h, n_w h] \times [-n_w h, n_w h]$ in the domain $D = [-10, 10] \times [-10, 10]$, discretized by $h = 0.025$, using the three quadratures defined above, T^2 , T^4 and T^6 , as a function of n_w . The figure shows that smaller values of n_w yield larger errors, as expected, and that the errors are smaller using higher order trapezoidal rules. Thus the size of the window that should be used depends on the desired size of the error. To reduce the acceptable size we use T^6 instead of T^4 . The final approximation thus used in this paper is

$$\int_D G \approx T_D^4[G] + E_W^6[H] \tag{3.29}$$

where $E^6[H] = \int H - T^6[H]$. The size of the window used in the results shown below ranges from $n_w = 5$ for $n \leq 80$ and $n_w = 9, 15, 26$ for $n = 160, 320, 640$, respectively.

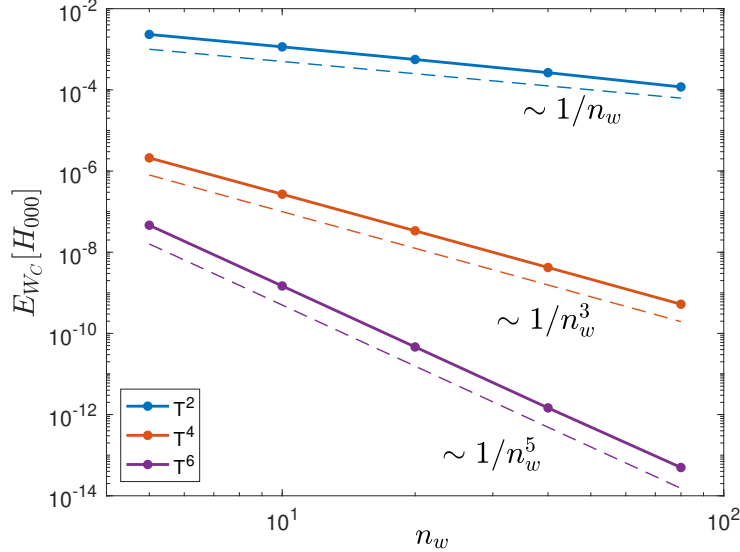


Figure 4: Error in the numerical integration of $H_{000} = 1/\sqrt{x^2 + y^2 + d^2}$ with $d = 0.001$ over the complement $W_C = D \setminus W$, where $W = [-n_w h, n_w h] \times [-n_w h, n_w h]$, $D = [-10, 10] \times [-10, 10]$ and $h = 0.025$, as a function of n_w , using the 2nd, 4th and 6th order Trapezoid rules T^2, T^4, T^6 , as indicated.

3.7. Minimizing Roundoff Error

The method consists of obtaining accurate results by adding a correction to a bad result. If the bad result is large, the correction is large, resulting in subtraction of two large numbers to obtain a more accurate much smaller number. This leads to loss of significant digits. This effect is more visible in calculations of the DLP, since the maximum uncorrected errors are larger, $O(h^2/d^2)$, than for the SLP, where they are $O(h^2/d)$. Figure 5(a) shows the error in calculating the double layer $D[\mathbf{f}](\mathbf{x}_0)$ for a sphere with $\mathbf{f} = (1, 0, 0)$ and \mathbf{x}_0 inside the sphere, for which the integral is known to be $(-1, 0, 0)$. It shows both the uncorrected error (dashed curves) and the error after adding the correction $E^6[H]$ (solid curves), for a range of values of $h = 2\pi/n$, where n is as indicated. For each h , it shows the maximum errors at distance d from the surface. The uncorrected error behaves as expected, like h/d^2 , for each h . The corrected errors are up to 10^{11} times smaller, and are almost constant in d . However, there is loss of accuracy for $n \geq 80$ as $d \rightarrow 0$. This loss of accuracy is caused by subtraction of like numbers in (3.29), when the values of $T^4[G]$ and $E^6[H]$ are large and almost equal in magnitude, but of opposite sign. Specifically, if we denote the trapezoidal rule as

$$T[G] = \sum_{j,k} G_{j,k} h^2 \quad (3.30)$$

then the loss of significance is due to the subtraction $G_{j_0,k_0} h^2 - H_{j_0,k_0} h^2$ at the grid point \mathbf{x}_{j_0,k_0} closest to the target point \mathbf{x}_0 .

This issue can be resolved by omitting the terms $G_{j_0,k_0} h^2$ and $H_{j_0,k_0} h^2$ from the trapezoidal rule summations. In practice, this amounts to replacing the trapezoidal rule in $T_D[G]$

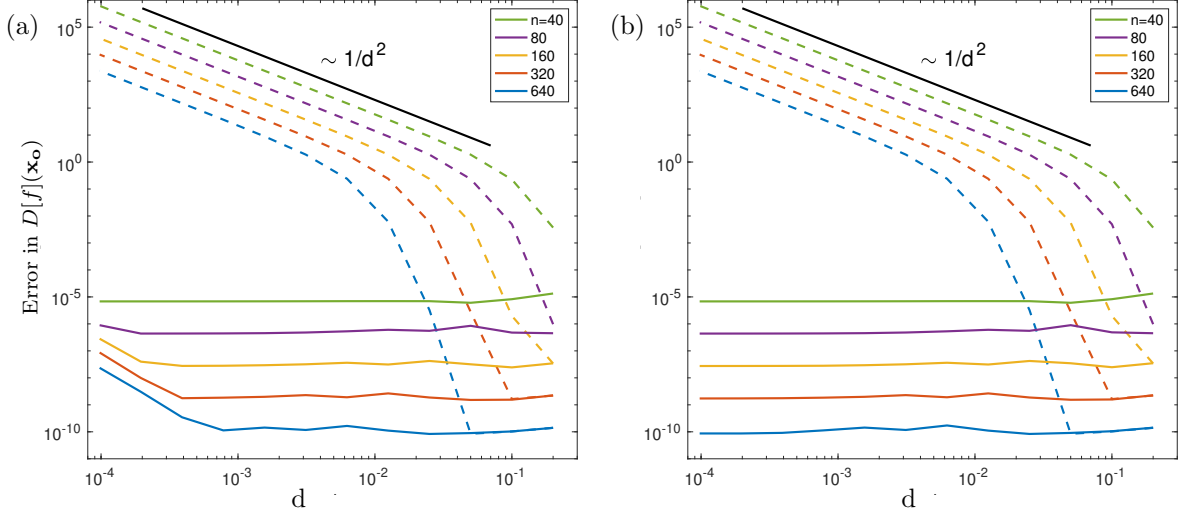


Figure 5: Maximal error in $D[\mathbf{f}](\mathbf{x}_0)$ with $\mathbf{f} = (1, 0, 0)$ and \mathbf{x}_0 inside sphere at distance d from the surface, vs d . The integral is computed with the uncorrected trapezoid rule $T^4[G]$ (dashed curves) and after adding the correction $E^6[H]$ (solid curves), with several values of $h = 2\pi/n$, n as indicated. (a) Corrected results show loss of accuracy due to subtraction of like numbers when $d \ll 1$. (b) Corrected results are $O(h^4)$, uniformly in d , when the punctured trapezoidal rule is used.

and $T_W[H]$ by a “punctured trapezoidal rule,” which is a common strategy used in singular quadratures, see [24] for example. Figure 5(b) shows the removal of roundoff error by this process for the example introduced in figure 5(a). The error in figure 5(b) is $O(h^4)$, decaying from 10^{-5} to 10^{-10} as h decreases by a factor of 16. In particular, the error converges *uniformly* in d .

We now present the analysis to justify the use of the punctured trapezoidal rule. First note that when $(j, k) = (j_0, k_0)$ and $\hat{\alpha}, \hat{\beta} \approx 0$, we have $\rho_0 \approx d$ in (3.12). For a function G of the form (3.17) with $F \sim d^m$ for some $m < r$, we have

$$G_{j_0, k_0} h^2 \sim \frac{F\omega}{\rho_0^r} \Big|_{(\alpha_{j_0}, \beta_{k_0})} h^2 \sim d^{m-r} h^2 \rightarrow \infty \text{ as } d \rightarrow 0. \quad (3.31)$$

By the expansion (3.15) and the truncation condition (3.20), $G - H$ is a remainder of the expansion containing basis functions H_{pqk} that satisfy $p + q - (2k + 1) \geq 2$, such that

$$H_{pqk} \Big|_{(\alpha_{j_0}, \beta_{k_0})} = \frac{\hat{\alpha}^p \hat{\beta}^q}{\rho_0^{2k+1}} \Big|_{(\alpha_{j_0}, \beta_{k_0})} = O(d^{p+q-(2k+1)}) = O(d^2) \quad (3.32)$$

Combining this fact with the Taylor Theorem one can show that $(G - H)_{j_0, k_0} = O(d^2)$, which implies

$$(G - H)_{j_0, k_0} h^2 = O(d^2 h^2). \quad (3.33)$$

Thus (3.31) and (3.33) shows that $G_{j_0, k_0} h^2 - H_{j_0, k_0} h^2$ is indeed a subtraction of two large numbers that cancel to 0 as $d \rightarrow 0$, whereas ignoring these terms in $T_D[G]$ and $T_W[H]$ only introduces an $O(d^2 h^2) = O(h^4)$ error, since $d = O(h)$.

On the other hand, when $(j, k) \neq (j_0, k_0)$, evaluating $(G - H)_{j,k}h^2 = G_{j,k}h^2 - H_{j,k}h^2$ does not lead to loss of significance. Note that in this case $|(\hat{\alpha}, \hat{\beta})| = |(\alpha_j - \alpha_b, \beta_k - \beta_b)| \geq h/2$, thus $\rho_0 \geq \sqrt{d^2 + c \cdot (h/2)^2} > \frac{\sqrt{c}}{2}h$ where $c > 0$ is the minimum singular value of a positive definite matrix associated with the quadratic form in (3.12); see also Appendix B. Thus the size of $G_{j,k}h^2$ (and likewise $H_{j,k}h^2$) is estimated to be

$$G_{j,k}h^2 \sim \frac{F\omega}{\rho_0^r} \Big|_{(\alpha_j, \beta_k)} h^2 = O(d^m h^{-r} h^2) = O(h^{m-r+2}). \quad (3.34)$$

So $G_{j,k}h^2$ and $H_{j,k}h^2$ are bounded for all d if $m - r + 2 \geq 0$, which is the case for the integrals considered in this paper.

3.8. Implementation

The following steps are taken to implement the method described above to compute the SLP and DLP $\mathcal{S}[\mathbf{f}](\mathbf{x}_0)$, $\mathcal{D}[\mathbf{f}](\mathbf{x}_0)$ over the surface of an ellipsoid E with major axes a, b, c in arbitrary location. Let a denote the largest major axis. Let h be the chosen mesh size. We also include references to the earlier relevant sections in each step.

Step 1. Standardize E and determine grid.

- 1a.** Rotate ellipse E and \mathbf{x}_0 to standard position \tilde{E} (§3.2).
- 1b.** Determine which grid to use: Check if $\tilde{\mathbf{x}}_0$ is closer to poles of grid 1 or of grid 2. Choose the grid whose poles it is further away from (§3.2). The density \tilde{f} has been precomputed and is given on both grids. Since the flow is steady, it stays constant in time.

Step 2. Determine if correction is needed. If not, compute $T[G]$. Done.

2a. Determine if a correction may be needed:

- (i) Obtain an upper bound d_{up} for the distance of $\tilde{\mathbf{x}}_0$ to \tilde{E} from the largest distance between the ellipsoid \tilde{E} and the ellipsoid with equal ellipticity through $\tilde{\mathbf{x}}_0$. If $d_{up} > 6ah$ set `correct=false`. Else, proceed to (ii).
- (ii) Find the orthogonal projection \mathbf{x}_b : starting from a nearby grid point, the nonlinear equation $(\mathbf{x}_b - \mathbf{x}_0) = d\mathbf{n}$, such that $\mathbf{x} \in S$, is solved using Newton's method. Find d . If $d < 6ah$, set `correct=true`. Else, set `correct=false`. The value of 6 is empirical and consistent with that used in other studies in the literature.

2b. If (`not correct`) set $\int G = T^4[G]$ (§3.5) and done. Else, continue with steps 3-5.

Step 3. Set `roundoff` and compute $T[G]$, punctured or not.

- 3a.** Let Δs be a characteristic grid size on the surface S near the basepoint \mathbf{x}_b . Determine whether $d < \Delta s/4$ and $\min_{j,k} |\mathbf{x}_b - \mathbf{x}_{j,k}| < \Delta s/4$. If so, set `roundoff=true`.

- 3b.** If (**not roundoff**), compute the trapezoid sum $T[G] = T^4[G]$. If (**roundoff**), compute the punctured sum obtained by skipping (j_0, k_0) term (§3.7).

Step 4. Compute $E[H_{pqk}^6]$ and c_{pqk}

- 4a.** Compute all derivatives of $\mathbf{x}, F, J, \mathbf{f}$ at (α_b, β_b) . Compute the coefficients $c_\alpha^2, c_{\alpha\beta}, c_\beta^2$. The derivatives of \mathbf{x}, F, J at the base point are given analytically. The derivatives of \mathbf{f} are obtained by bi-cubic interpolation of the given values at the grid points.
- 4b.** Compute $E[H_{pqk}]$. Note that the functions H_{pqk} depend only on the base point (α_b, β_b) , the distance d and the coefficients $c_\alpha^2, c_{\alpha\beta}, c_\beta^2$.
- (i) Set the window W using a pre-determined value of n_w (§3.6).
 - (ii) Compute $\int_W H_{pqk}$ using the recursive algorithm (§3.4).
 - (iii) Compute $T_W^6[H_{pqk}]$. If (**roundoff**), skip the (j_0, k_0) term (§3.5).
 - (iv) Set

$$E^6[H_{pqk}] = T_W^6[H_{pqk}] - \int_W H_{pqk}$$

- 4c.** Compute all coefficients c_{pqk} . These are obtained by multiplying the corresponding coefficients of the expansions of F, J, f and η^l for the proper value of l .

Step 5. Set $\int G = T[G] + E^6[H]$, where $E^6[H] = \sum_{pqk} c_{pqk} E^6[H_{pqk}]$ (§3.1).

4. Numerical results

In this section we apply the corrected quadrature $T^4[G] + E^6[H]$ to compute Stokes flow past several objects, and compare with results using the uncorrected trapezoidal rule $T^4[G]$. The goal is to show the accuracy of the corrected values, and the severity of the errors in the absence of corrections.

4.1. Stokes flow past sphere

Our simplest example is flow past a sphere of unit radius with constant far field velocity \mathbf{u}_∞ of unit magnitude. Here, the density $\mathbf{f} = -1.5\mathbf{u}_\infty$ and the fluid velocity are known explicitly [18], making comparison with exact solutions possible. In addition, the parametrizations (3.6) are orthogonal, with $c_{\alpha\beta} = 0$ (3.13), thus reducing sources of error. Finally, for constant density and target points outside the sphere the DLP vanishes. We thus set

$$\mathbf{u}(\mathbf{x}_0) = \mathcal{S}[\mathbf{f}](\mathbf{x}_0) + \mathbf{u}_\infty \tag{4.1}$$

and solely test the SLP. Results solely for the DLP were shown earlier, in Fig. 5. Throughout this section, the mesh used is defined by n , where $n_1 = n_2 = n$, $m_1 = m_2 = n/2$. To avoid grid imprinting, the far field is chosen to be at a 45° degree angle from the equator, $\mathbf{u}_\infty = (1, 0, -1)/\sqrt{2}$.

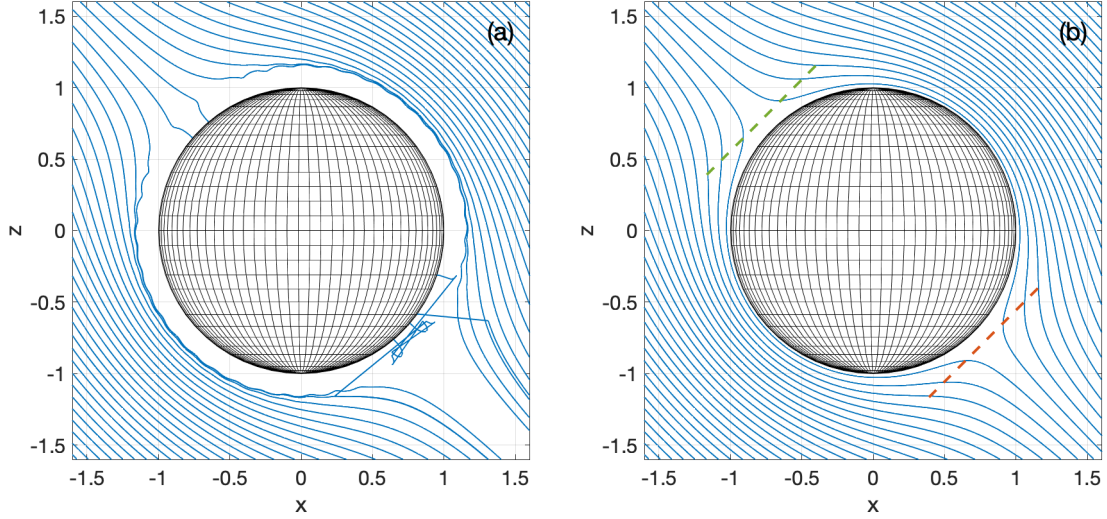


Figure 6: Streamlines in the plane $y = 0$, obtained by integrating the velocity field with RK4 and $\Delta t = 0.1$. The velocity is computed with $n = 40$, without corrections in (a) and with corrections in (b). The green and red dashed lines in (b) are included for later reference.

Figure 6 plots the streamlines past the sphere in the cross section $y = 0$. They are computed by integrating the velocity field using the 4th order Runge Kutta method (RK4) with $\Delta t = 0.1$, which is sufficiently small that results are resolved in time. The velocity is computed using $n = 40$, without corrections in figure (a), and with corrections in figure (b). The uncorrected velocity in (a) has large errors near the boundary, and the streamlines within that region are not resolved. Most streamlines stay outside a layer around the sphere and do not properly approach it. Some streamlines enter the sphere. The streamlines with the corrected velocity, in figure (b), appear well resolved, even close to the boundary.

Figure 7 more clearly shows the magnitude and distribution of the error in the computed velocity. Figure (a) plots the maximum error at fixed distance d from the surface, for a range of values of d and several mesh sizes $h = 2\pi/n$, with n as indicated. The maximum error is evaluated by sampling the error over 320^2 points in $(\alpha, \beta) \in [0, \pi/4] \times [0, \pi/4]$. The uncorrected errors (dashed curves), satisfy the expected scaling $O(h^2/d)$. The corrected errors (solid curves) are several orders of magnitude smaller and are uniformly $O(h^4)$ as $d \rightarrow 0$. Figures 7(b,c) show the distribution of the uncorrected and corrected errors at a fixed distance $d = 0.0001$ from the surface, with $n = 40$. The maximum uncorrected errors in Fig.7(b) occur at target points placed directly above the grid points. The corrections in Fig.7(c) significantly reduce the size of the errors. In (c) one can also distinguish the two grids used by different target points. Targets closer to the poles $(0, 0, \pm 1)$ use grid 2, while targets closer to $(\pm 1, 0, 0)$ use grid 1.

Figure 8 presents an alternative approach to measure the incurred error that will be useful below, when considering flow past several objects. We track the motion of particles under the computed velocity field as they move from a region on the windward side of the sphere, where the flow is coming from, to the other, leeward, side, and compute the integral

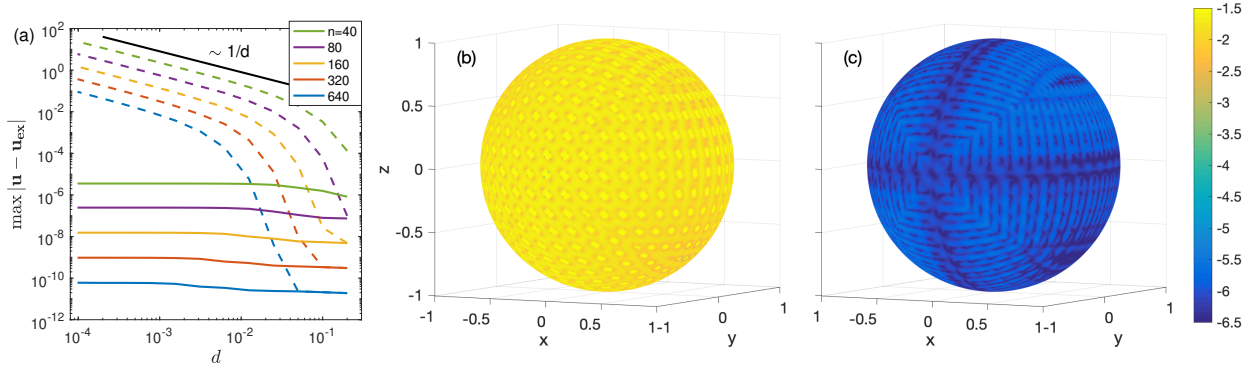


Figure 7: (a) Maximal error in the velocity past the sphere at distance d from the surface, vs d . The velocity is computed without corrections (dashed curves) and with corrections (solid curves), using the indicated values of n . A line proportional to $1/d$ is shown as reference. (b,c) Distribution of error on sphere, with $n = 40$, at fixed distance $d = 0.0001$, computed without corrections in (b) and with corrections in (c), on a logarithmic scale.

error incurred in the particle position and in the time it takes to traverse the region. We note that the time of traversal in viscous flow through a porous media is a quantity of interest in applications, as studied for example in [5].

Specifically, we place 75^2 particles on a square of size 0.9×0.9 normal to the incoming flow at distance 0.1 from the sphere. This square is indicated in Fig.6(b) by the green dashed line. The particle motion is computed using RK4 with sufficiently small timesteps to yield resolved results (here, $\Delta t = 0.02$), and we record the time T_{fin} and position \mathbf{y}_{fin} when the particles have reached a plane parallel to the windward square on the leeward side, at distance 0.1 from the sphere, indicated by the red dashed line in Fig.6(b). The particles are evolved using the uncorrected velocity and the corrected velocity with $n = 40$, and using the exact velocity, as reference.

Figures 8(a,b) plot the particles traversal time T_{fin} as a function of their initial position in the windward plane, using the uncorrected velocity in (a) and the corrected velocity in (b), on a logarithmic scale. The results in (b) are indistinguishable from those obtained with the exact velocity. Only one quarter of the region is shown, since the result in the remaining quarters are approximately equal by symmetry. The particles near $(y_0, z_0^*) = (0, 0)$ are closest to the windward stagnation point and take the longest time to reach the leeward side. As seen in (b), the times decrease radially outwards. The difference between (a) and (b) reflects the integral error made along streamlines by the uncorrected rule in the total time it takes to traverse the sphere. The white squares in (a) correspond to points that never reach the leeward plane.

Figures 8(c,d) plot the error in the position \mathbf{y}_{fin} of the particles once they reach the leeward plane. The error is obtained by comparison with the exact values, which follow from the reversibility of Stokes flow. Results using the uncorrected velocity in (c) show relatively large errors in the position for a significant subset of points. Again, the white squares indicate points that never reach the leeward plane.

Figures 9(a,b) plot the same information as Fig.8 in a more quantitative way. Figure 9(a)

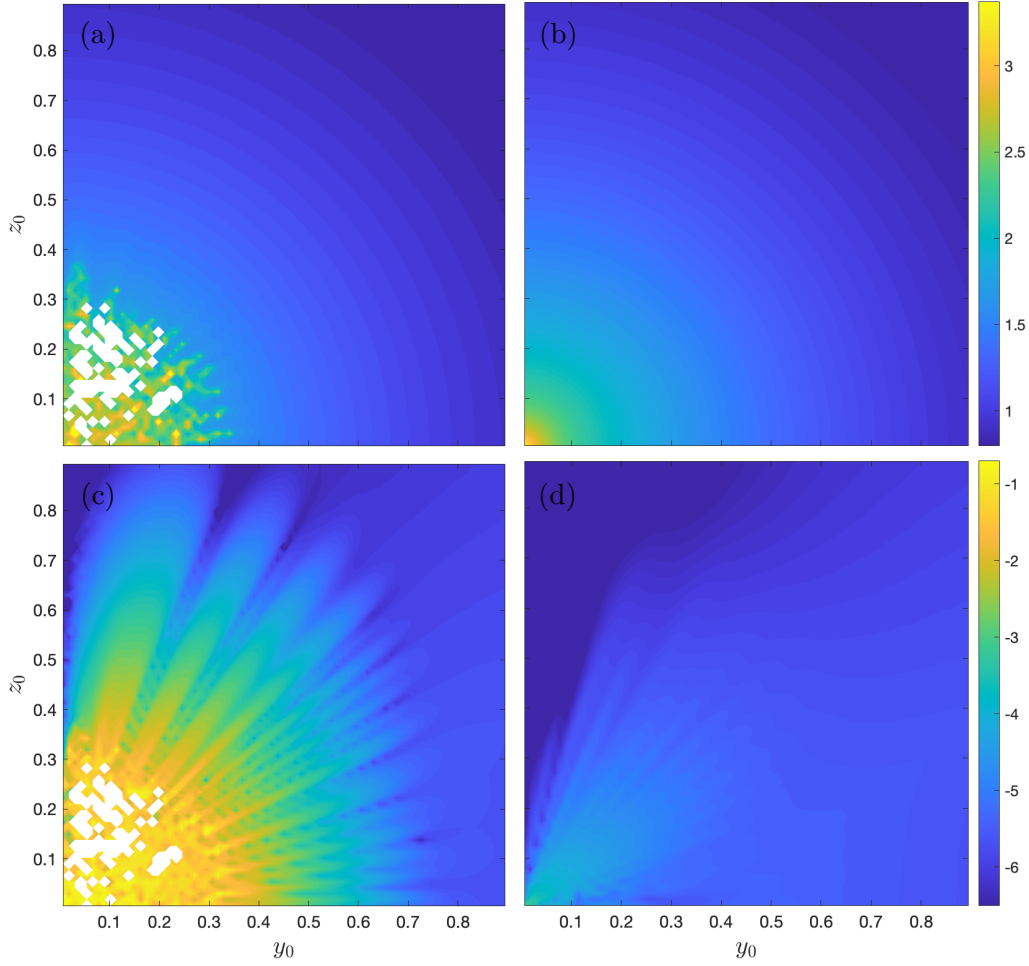


Figure 8: Particles initially positioned in the square $[y_0, z_0] = [0, 0.9] \times [0, 0.9]$ in the plane $x - z = -1.1$ are evolved with the fluid velocity until they reach the plane $x - z = 1.1$ (a,b) Time T_{fin} taken by the particles, as a function of their original coordinates. (c,d) Error $E[Y_{fin}]$ in the final position of the particles. (a,c) are computed using the uncorrected velocity, (b,d) use the corrected velocity.

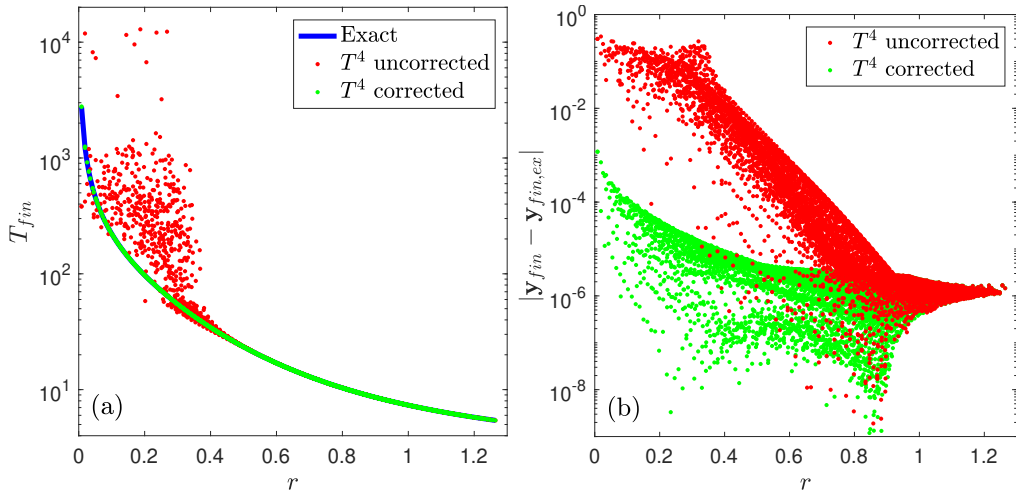


Figure 9: Scatter plots of (a) T_{fin} and (b) $E[Y_{fin}]$ as a function of $r = |(y_0, z_0)|$, computed with the exact velocity, the uncorrected velocity, and the corrected velocity, as indicated.

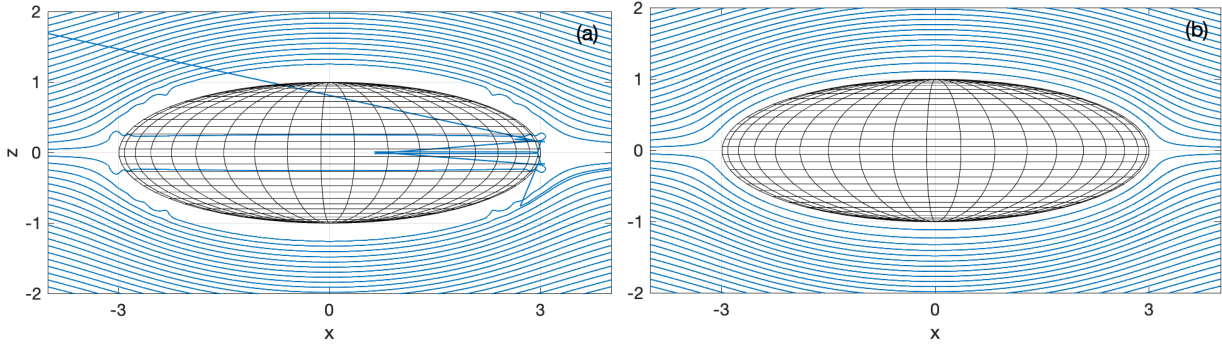


Figure 10: Streamlines around a 3-2-1 ellipsoid in the plane $y = 0$. The velocity is computed with $m = 20$, without corrections in (a) and with corrections in (b).

presents a scatter plot of the traversal time of all particles, computed with the uncorrected (red), corrected (green), and exact velocity (blue), as a function of the radial coordinate $r = |(y_0, z_0^*)|$. The scatter of the red dots shows many points for which the uncorrected velocity results in traversal times more than 100 times larger than the actual values. Figure 9(b) shows the error in the position of each particle, as a function of r . While the cumulative errors using the corrected velocity increase towards the center, $r = 0$, where the traversal times are longer, they are less than 10^{-3} in all cases. The errors using the uncorrected velocity are often 100-1000 times larger.

4.2. Flow past ellipse

We now consider a standard ellipsoid (3.5) with major axes $(a, b, c) = (3, 2, 1)$ in a far-field $\mathbf{u}_\infty = (1, 0, 0)$. This case adds complexity to the previous example: (i) The density is not known analytically. It and all its derivatives are precomputed at the grid points as described in §2. The values at the base point \mathbf{x}_b required for the coefficients c_{pqk} are obtained by interpolation. (ii) The latitude-longitude grids are no longer orthogonal, so that $c_{\alpha\beta} \neq 0$. Thus the recursion in section §3.4 is necessary to compute $\int H_{pqk}$. (iii) The DLP is not zero. (iv) The exact solution is not known. Here, the mesh used is defined by m with $n_1 = 4m, m_1 = m, n_2 = 3m, m_2 = 2m$. We use the solution with $m = 320$ as a reference to compute errors shown below.

Figures 10(a,b) show streamlines of the flow in the cross section $y = 0$, computed by integrating the velocity using RK4. The velocity is computed with $m = 20$, without corrections in (a), and with corrections in (b). Similarly to Fig. 6, the errors in (a) are large near the body. Either streamlines stay bounded away from the body, or they enter the body. Figure 10(b) shows resolved results.

Figures 11(a,b) plot the errors in the velocity in the same cross section as above, computed with $m = 20$, inside and outside the ellipse, without corrections in (a) and with corrections in (b), on a logarithmic scale. Figure 11(a) clearly shows large errors in the uncorrected velocity near the boundary of the ellipsoid. The maximum errors are of the order of 10^6 , as shown next, and occur near the grid points. The target points using the two distinct grids are clearly visible, since the chosen resolution on grid 2 is finer than on grid 1; we have not

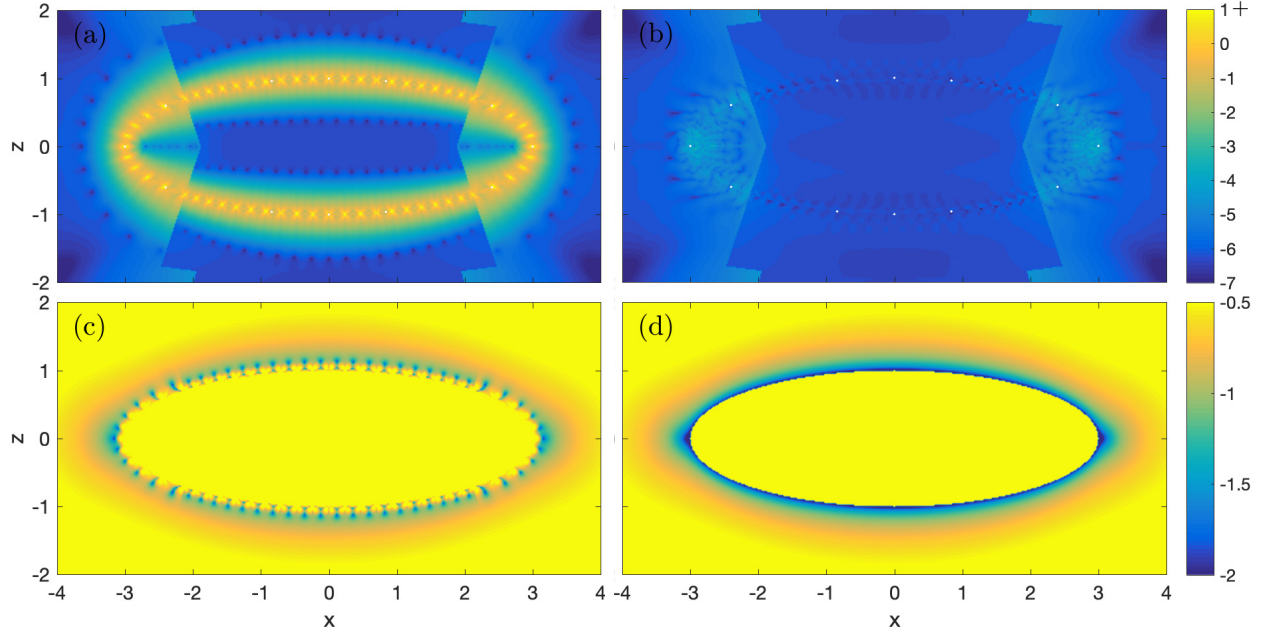


Figure 11: Velocity in the plane $y = 0$. (a,b) Error $|\mathbf{u} - \mathbf{u}_{\text{ex}}|$, and (c,d) velocity magnitude $|\mathbf{u}|$, all on a logarithmic scale. Computed with $m = 20$, without corrections in (a,c) and with corrections in (b,d). The symbol 1+ on the colorbar indicates that actual values may be bigger than 10.

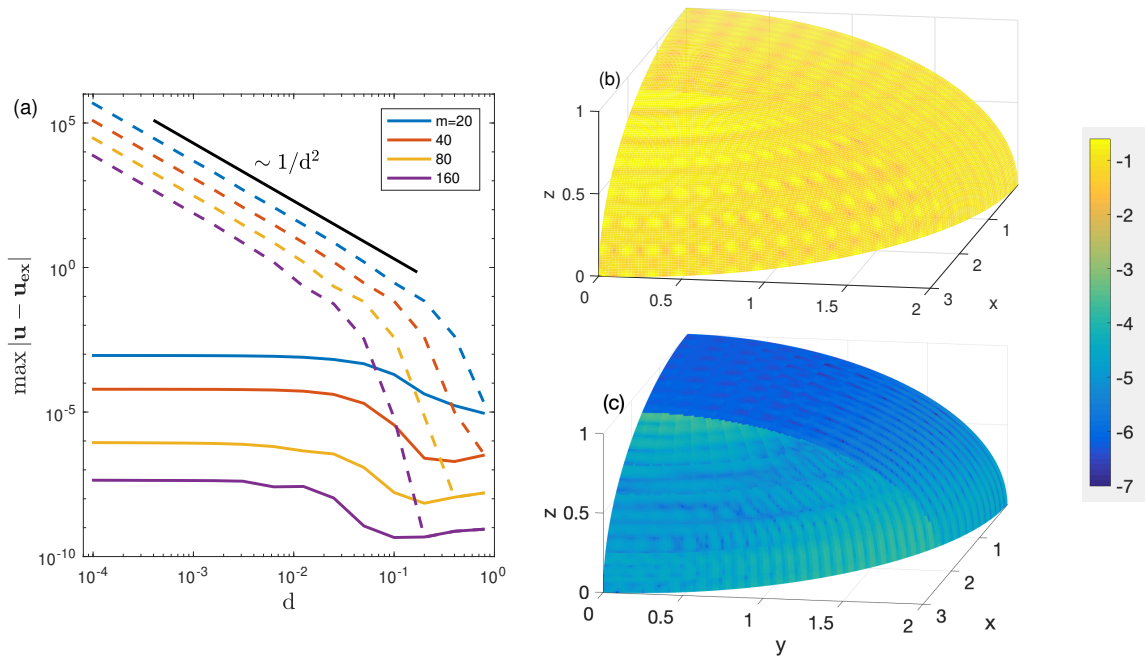


Figure 12: (a) Maximal error in the velocity past the ellipse at distance d from the surface, vs d , computed without corrections (dashed curves) and with corrections (solid curves), using the indicated values of m . (b,c) Distribution of error on an octant of the ellipse at distance $d = 0.1$, computed with $m = 20$, without corrections in (b) and with corrections in (c).

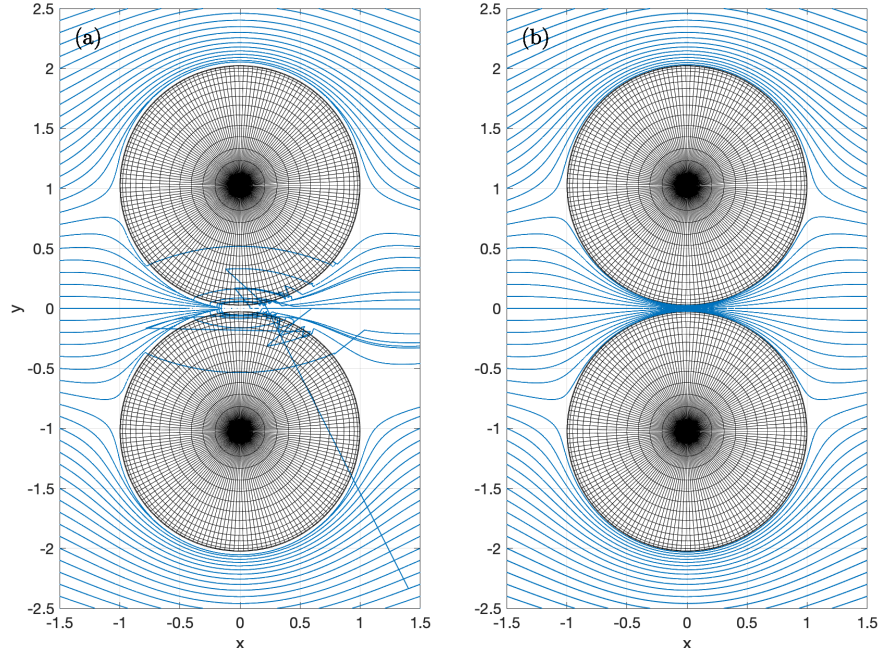


Figure 13: Streamlines around two spheres separated by $d = 0.05$, in the plane $z = 0$, computed with $n = 320$. The density and velocity are computed without corrections in (a), and with corrections in (b).

optimized the two meshes to match the error size. Figure 11(b) shows the error after adding corrections. The maximum errors are 10^{-3} . Figures 11(c,d) plot the corresponding velocity. In (c), the uncorrected velocity does not accurately resolve zero flow at the wall. The corrected velocity in (d) clearly resolves the jump in the double layer across the boundary.

The error as a function of the resolution and its spatial distribution is more clearly shown in Fig. 12. Figure 12(a) plots the maximum errors in the velocity computed without corrections (dashed lines) and with corrections (solid lines), at distance d from the surface, with the indicated values of m . The uncorrected errors satisfy the scaling $O(h^2/d^2)$, as expected for the double layer. With corrections, the errors are reduced by factors $10^9 - 10^{11}$. The corrected errors are $O(h^4)$, where $h = \pi/m$, uniformly as $d \rightarrow 0$.

Figures 12(b,c) show the spatial distribution of errors at a fixed distance $d = 0.1$, computed with $m = 20$, without and with corrections. As before, the two different grids used, depending on the target point, are evident, with smaller errors on grid 2 since the chosen resolution there is finer.

4.3. Stokes flow past 2 spheres

Next, we consider flow past two spheres of radius 1, centered at $(0, \pm(1 + d/2), 0)$, with far-field $\mathbf{u}_\infty = (1, 0, 0)$, with a gap of size $d = 0.05$ between them. In this case, solving for the density on one sphere S_1 requires accurate evaluation of the velocity induced by the other sphere S_2 on the boundary of S_1 . These integrals are near-singular for points on the boundary of S_1 near S_2 . Thus, accurate evaluation of the near-singular integrals is required both to obtain the density as well as to compute the fluid velocity induced by that density.

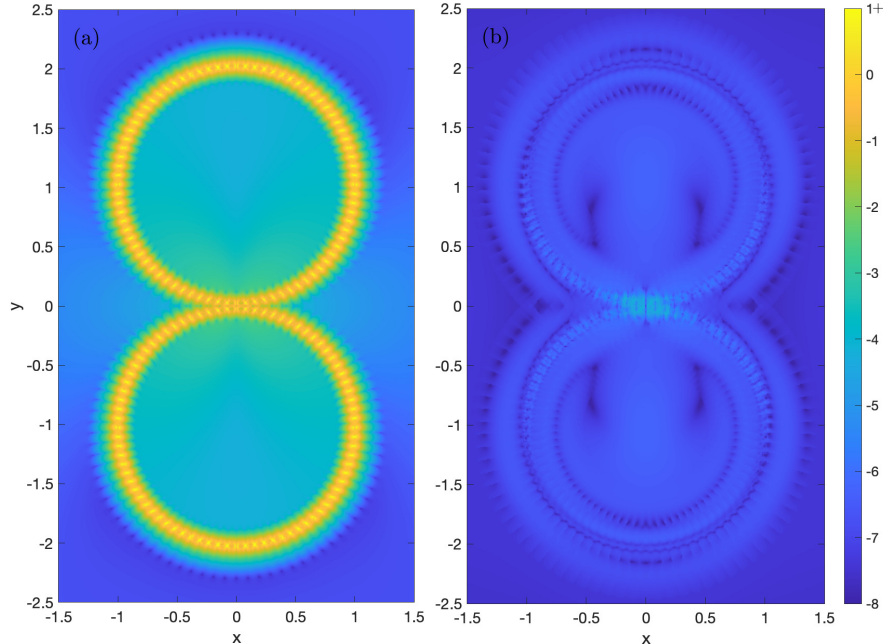


Figure 14: Velocity error $|\mathbf{u} - \mathbf{u}_{\text{ex}}|$ in the plane $z = 0$, computed with $n = 80$, without corrections in (a), and with corrections in (b), on a logarithmic scale.

Figure 13 shows the resulting streamlines in the x - y plane, where the velocity is computed with $n = n_1 = n_2 = 320$, $m = n/2$. As before, streamlines are obtained by integrating the computed velocity using RK4 and sufficiently fine timesteps. In Fig. 13(a), both the density and the velocity are computed without corrections, while in (b) they are computed with corrections. Figure 13(a) shows that the velocity is inaccurate in a thin layer around both spheres, in which the streamlines do not hug the boundary sufficiently closely, and highly inaccurate in the narrow gap between the spheres. Many streamlines unphysically enter the spheres. Figure 13(b) shows accurate streamlines around both spheres, and in the narrow gap between them. The relatively high resolution of $n = 320$ was necessary to resolve the flow in the gap.

Figure 14 plots the error in the velocity, computed at lower resolution $n = 80$, without corrections in (a), and with corrections in (b). The error is obtained by comparison with $n = 320$ results. The plots show the significant reduction in the error by adding the corrections. The corrected error is largest in the gap between the spheres, where the boundary density is larger in magnitude and less well resolved.

4.4. Flow past several ellipsoids

The last example is that of flow past three ellipsoids, positioned somewhat randomly, but so that they are close to each other. Their centers (x_c, y_c, z_c) , semi-axes lengths a, b, c , and orientation angles (ϕ, θ, ψ) , are given in table 1. The corresponding gaps between any two of these ellipsoids, defined as the smallest distance between them, range between 0.21 and 0.25, which are less than 5% of the diameters of the ellipsoids. Table 1 also lists the

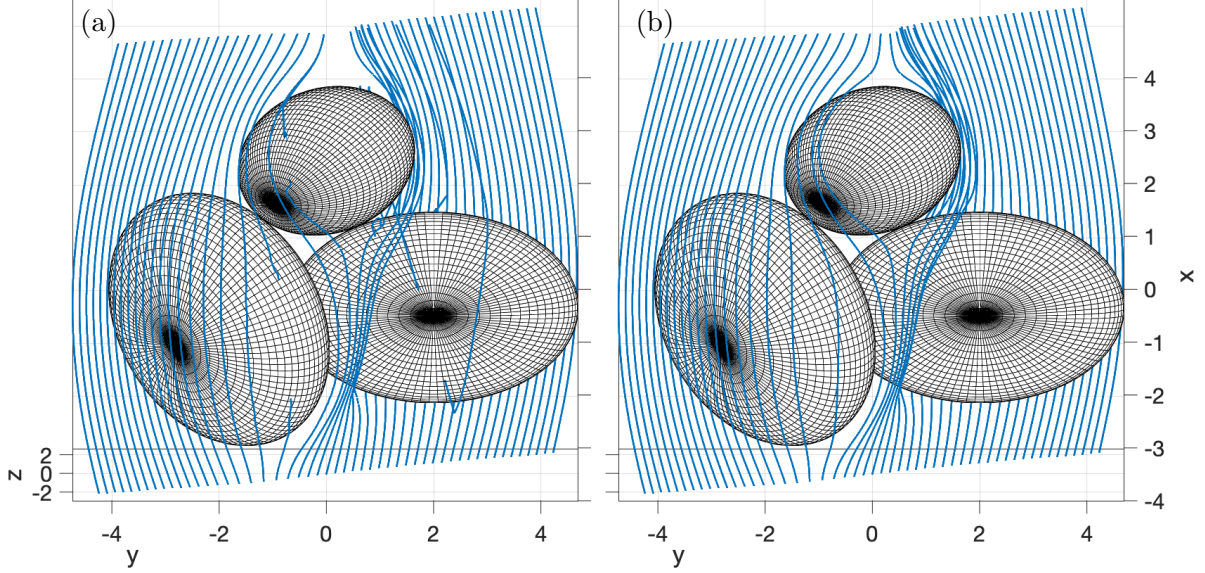


Figure 15: Streamlines past the three ellipsoids, initialized on a line in the plane $x = -3$. Velocity and densities are computed with the discretization listed in table 1, without corrections in (a), and with corrections in (b).

discretization values m_1, n_1, m_2, n_2 used in all the results shown below. The background velocity is $\mathbf{u}_\infty = (1, 0, 0)$.

Figures 15(a,b) plot streamlines past the ellipsoids, obtained by integrating the velocity field, where velocity and density are computed without corrections in (a), and with corrections in (b). The streamlines shown are initialized on a line in the plane $x = -3$, with the flow moving upward (positive x -direction). In (a), several streamlines enter the objects, and a large gap between streamlines is visible behind the smallest ellipsoid. The streamlines in (b) appear resolved.

One measure of the error in the velocity field is shown in Fig. 16. It plots the error magnitude in the plane through the three points closest to each pair of ellipsoids. In figure (a), the velocity and the densities are computed without corrections; in figure (b), they are computed with corrections. The error is obtained by comparing with results obtained with a mesh three times as fine. The uncorrected velocity in Fig.16(a) has large errors near the ellipsoid boundary, with maximal value 72.1. The corrected results in figure (b) are significantly better resolved, with maximal error 9.7×10^{-4} .

	a, b, c	x_c, y_c, z_c	ϕ, θ, ψ	m_1, n_1	m_2, n_2
Ellipsoid 1	1.80, 2.70, 0.90	-0.95, 2.0, 0.5	0, 0, 0	20,80	32,98
Ellipsoid 2	2.50, 2.50, 1.25	-1.0, -2.0, -0.5	$\frac{\pi}{3}, \frac{\pi}{4}, \frac{7\pi}{8}$	20,80	40,80
Ellipsoid 3	2.70, 1.35, 1.35	2.0, 0.0, -0.5	$\frac{\pi}{2}, -\frac{\pi}{3}, -\frac{\pi}{5}$	30,60	42,42

Table 1: Parameters describing positions and discretizations of three ellipsoids.

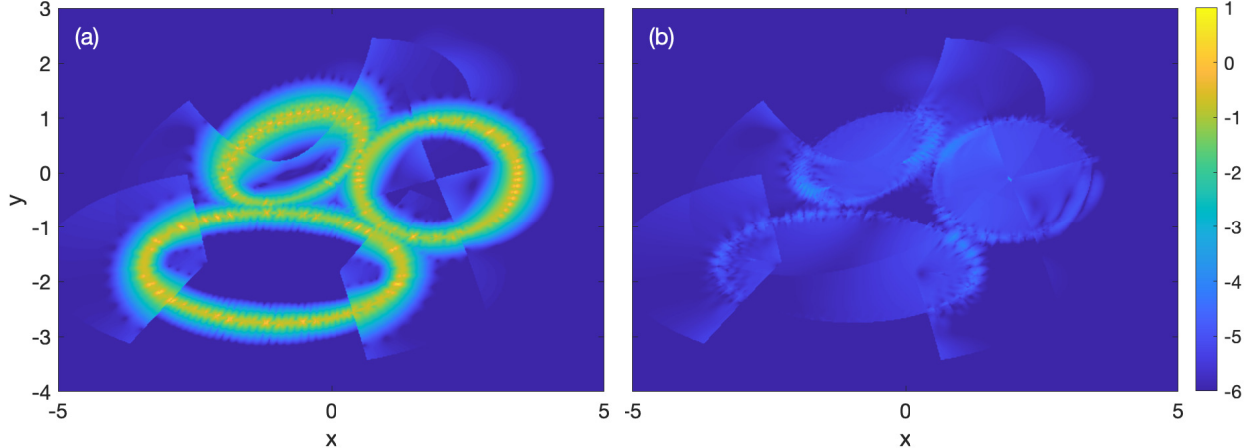


Figure 16: Velocity error $|\mathbf{u} - \mathbf{u}_{ex}|$, in a plane through the 3 points closest to each pair of ellipsoids, projected onto the x - y plane, on a logarithmic scale. The velocity and densities are computed with the discretization listed in table 1, without corrections in (a), and with corrections in (b).

A more complete measure is the integral error in the shadow of the ellipsoids, shown in Figs. 17 and 18. Similar to Fig. 8, we place a set of particles in a plane upstream of the ellipsoids, and measure errors in the time and position of those particles when they reach a parallel plane downstream of the ellipsoids. Here, we place 40^2 particles in a square in the plane $x = -3.6$ with side length 6 centered at $(y_c, z_c) = (0.35, -0.5)$. The initial particle position is given by their coordinates $\mathbf{y}_0 = (y_0, z_0)$ in this plane. We then compute the trajectory of those particles by integrating the velocity field using RK4 with a sufficiently small timestep, and record the time T_{fin} and their positions $\mathbf{y}_{fin} = (y_{fin}, z_{fin})$ when they reach $x = 3.6$.

Figures 17(a,b) plot the time T_{fin} as a function of the initial position \mathbf{y}_0 , on a logarithmic scale, where velocity and densities are computed without corrections in (a), and with corrections in (b). The white squares in figure (a) correspond to particles that never make it across due to large errors in the uncorrected velocity. With the corrected velocity, all particles reach the downstream plane. The plus sign on the color bar indicates that there are particles, those that travel closest to the ellipsoids, that take more than $10^{2.6}$ time units to move across, as shown next. The shape of the yellow region describing the particles that take the longest to traverse the region is, interestingly, in no clearly predictable correlation with the position of the ellipsoids.

Figures 17(c,d) plot the displacement $|\mathbf{y}_{fin} - \mathbf{y}_0|$, using the uncorrected density and velocity in (c) and corrected values in (d). The speckled area in (c) represents the area where the errors are largest, similar to (a). The yellow area in (d) represents the points that are displaced most by traversing the ellipsoids. Again, this area is not clearly predictable based on the given geometry.

Figure 18 shows a scatter plot of the quantities in Fig.17. For every particle, it plots T_{fin} in (a), and the error in $|\mathbf{y}_{fin} - \mathbf{y}_0|$ in (b), vs the exact traversal time $T_{fin,ex}$, as obtained using a fine mesh. The green dots are the values computed with the corrected velocity, the

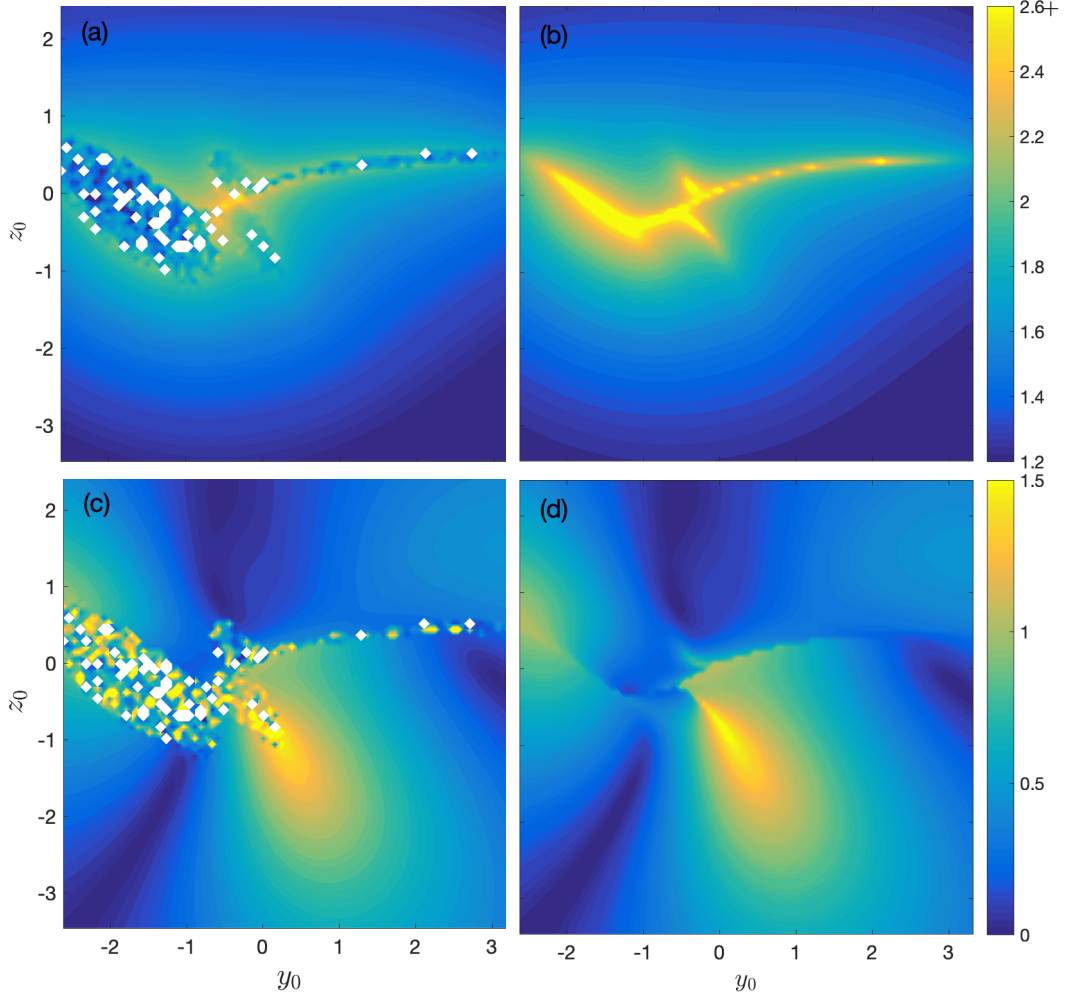


Figure 17: (a,b) Time T_{fin} and (c,d) displacement $|\mathbf{y}_{fin} - \mathbf{y}_0|$ of particles initially at $\mathbf{y}_0 = (y_0, z_0)$ in the plane at $x = -3.6$, after moving to $x = 3.6$, on a logarithmic scale. Velocity and densities are computed without corrections in (a,c), and with corrections in (b,d), using the mesh given in table 1.

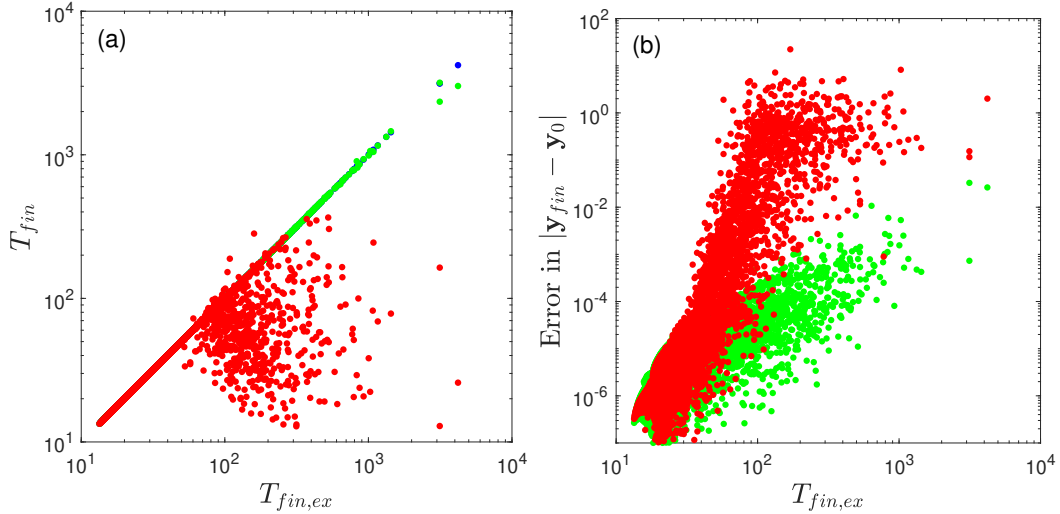


Figure 18: Scatter plots of (a) T_{fin} and (b) error in the displacement $|\mathbf{y}_{fin} - \mathbf{y}_0|$, as a function of $T_{fin,ex}$. Corrected results are shown in green, uncorrected in red.

red dots are computed with the uncorrected velocity. In Fig.18(a), the blue markers indicate the line of exact results, $T_{fin} = T_{fin,ex}$. The green dots align well with the blue dots, with some discrepancy visible for large times $T_{fin,ex} \approx 10^3$. The red dots show the extent of the error incurred using the uncorrected velocity. These values are generally much smaller than the exact values, sometime more than 100 times smaller. With the uncorrected velocity the particles move faster around the ellipsoids since they do not approach the objects as closely, as was seen earlier for flow past a sphere (Fig.6) and past one ellipsoid (Fig.10). The data in Fig.18(b) shows that, when computed without corrections, the error in the particle position after traversing the ellipsoids is up to $10^4 - 10^5$ times larger than the correct values.

5. Conclusions

This paper presents a quadrature method for near-singular integrals (1.1) that arise in the Boundary Integral Equation method in 3D, for target points \mathbf{x}_0 close to the surface of integration. As a direct generalization of the quadrature of [15] from line integrals to surface integrals, we derive a high-order quadrature by error correction of the double Trapezoidal rule. The near-singular integrands are approximated by an expansion using basis functions that can be integrated to high accuracy with recursion formulas. Fourth-order corrected quadratures are derived for the Stokes kernels and their convergence is validated and analyzed at target points near a sphere or an ellipsoid. For any fixed discretization, uniform accuracy is achieved for all close targets regardless of their distance d to the surface. Proper care is taken to resolve the loss of significance due to roundoff effects as $d \rightarrow 0$. The quadratures are applied to simulate viscous flows past multiple objects (two spheres or three ellipsoids), where each pair of objects is separated by a small distance that is 2.5% - 5% of the object diameters.

Our quadrature correction scheme can be extended to accommodate a greater variety of problems, which may involve different integral operators and parametric surfaces of more general shapes. Corrections for the Laplace and Helmholtz kernels, with application to vortex flows and wave scattering problems, are currently being explored. In view of recent work [26], another interest is the development of easy-to-use integral equation solvers that unify near-singular and singular quadratures. Finally, replacing the Trapezoid rule by other quadratures could give higher flexibility to treat more general surfaces.

Appendix A. Recursion for $\int F_{pk}, G_{qk}$

The integrals

$$F_{pk} = \int_a^b \frac{u^p}{\rho_u^{2k+1}} du, \quad G_{qk} = \int_c^d \frac{v^q}{\rho_v^{2k+1}} dv, \quad (\text{A.1})$$

are evaluated recursively, as follows. Set

$$F_{00} = -\ln(-u - cv + \rho_u) \Big|_{u=a}^{u=b} \quad (\text{A.2a})$$

$$F_{0k} = \frac{1}{[(1-c^2)v^2 + 1](2k-1)} \left[\frac{u+cv}{\rho_u^{2k-1}} + 2(k-1)F_{0(k-1)} \right], \quad k = 1 : K \quad (\text{A.2b})$$

$$F_{p0} = \frac{1}{p} \left[u^{p-1} \rho_u - (2p-1)cvF_{(p-1)0} - (p-1)(v^2+1)F_{(p-2)0} \right], \quad p = 1 : M \quad (\text{A.2c})$$

$$F_{pk} = \frac{1}{2k-1} \left[-\frac{u^{p-1}}{\rho_u^{2k-1}} + (p-1)F_{(p-2)(k-1)} \right] - cvF_{(p-1)k}, \quad k = 1 : K, \quad p = 1 : M \quad (\text{A.2d})$$

where all F_{pk} with negative indeces are set to zero. The values of G_{qk} are computed similarly, by simply replacing F, u, p, a, b respectively by G, v, q, c, d above.

Appendix B. Positive definiteness of $c_\alpha^2 \alpha^2 + 2c_{\alpha\beta} \alpha\beta + c_\beta^2 \beta^2$

For given target point \mathbf{x}_0 and its orthogonal projection \mathbf{x}_b onto an ellipsoid $\mathbf{x}(\alpha, \beta)$, define the quadratic form

$$Q(\alpha, \beta) := A\alpha^2 + 2C\alpha\beta + B\beta^2 \quad (\text{B.1})$$

where the coefficients A, B, C are given by (using the notation of (3.13))

$$\begin{aligned} A &= c_\alpha^2 = (\mathbf{x}_b - \mathbf{x}_0) \cdot \mathbf{x}_{\alpha\alpha} + \mathbf{x}_\alpha \cdot \mathbf{x}_\alpha, \\ C &= c_{\alpha\beta} = (\mathbf{x}_b - \mathbf{x}_0) \cdot \mathbf{x}_{\alpha\beta} + \mathbf{x}_\alpha \cdot \mathbf{x}_\beta, \\ B &= c_\beta^2 = (\mathbf{x}_b - \mathbf{x}_0) \cdot \mathbf{x}_{\beta\beta} + \mathbf{x}_\beta \cdot \mathbf{x}_\beta, \end{aligned} \quad (\text{B.2})$$

The quadratic form is *positive definite* if $Q(\alpha, \beta) > 0$ for all $(\alpha, \beta) \neq (0, 0)$, or, equivalently, if $A > 0$, $B > 0$, and $C^2 < AB$.

Let \mathbf{n} be the outward unit normal at \mathbf{x}_b , and d be the signed distance from \mathbf{x}_0 to \mathbf{x}_b ,

$$\mathbf{x}_0 - \mathbf{x}_b = d\mathbf{n}, \quad (\text{B.3})$$

In this section we show that the quadratic form is positive definite provided \mathbf{x}_0 is either outside the ellipse, or if it is inside, at a distance $|d|$ smaller than the radius of the osculating sphere. The osculating sphere at \mathbf{x} is the largest sphere inside the ellipsoid that only intersect the ellipsoid at a single point \mathbf{x} . Under these conditions, $A > 0$ and $B > 0$, as shown in [15]. It remains to show that $C^2 < AB$.

We first define the following.

1. The coefficients of the first and second fundamental forms at \mathbf{x}_b are

$$\begin{aligned} E &:= \mathbf{x}_\alpha \cdot \mathbf{x}_\alpha, & F &:= \mathbf{x}_\alpha \cdot \mathbf{x}_\beta, & G &:= \mathbf{x}_\beta \cdot \mathbf{x}_\beta \\ L &:= \mathbf{n} \cdot \mathbf{x}_{\alpha\alpha}, & M &:= \mathbf{n} \cdot \mathbf{x}_{\alpha\beta}, & N &:= \mathbf{n} \cdot \mathbf{x}_{\beta\beta}. \end{aligned}$$

2. The mean curvature H and the Gaussian curvature K at \mathbf{x}_b are given by

$$H := \frac{EN - 2FM + GL}{2(EG - F^2)} \quad K := \frac{LN - M^2}{EG - F^2},$$

3. The principal curvatures at \mathbf{x}_b are

$$\kappa_1 := H - \sqrt{H^2 - K} \quad \text{and} \quad \kappa_2 := H + \sqrt{H^2 - K}.$$

The coefficients (B.3) can be written as

$$\begin{aligned} A &= E - Ld, \\ C &= F - Md, \\ B &= G - Nd. \end{aligned} \tag{B.4}$$

Then the positive definiteness condition $AB > C^2$ can be equivalently written as

$$1 - 2dH + d^2K > 0.$$

Solving the inequality above gives

$$\frac{1}{d} < \kappa_1 \quad \text{or} \quad \frac{1}{d} > \kappa_2. \tag{B.5}$$

Note that $d > 0$ when \mathbf{x}_0 is outside of the ellipsoid, and $d < 0$ when \mathbf{x}_0 is inside. Also, $\kappa_1 < \kappa_2 < 0$ at any \mathbf{x}_b on an ellipsoid.

For any point \mathbf{x}_0 outside the ellipsoid we have $d > 0$, thus (B.5) is satisfied and the quadratic form (B.1) is positive definite. On the other hand, if \mathbf{x}_0 is inside the ellipsoid, then $d < 0$, in which case (B.5) is satisfied when $|d| < 1/|\kappa_1|$. In that case also $A, B > 0$. Equation (B.5) is also satisfied when $|d| > 1/|\kappa_2|$, but in that case, A and B are not positive.

Note that $R_{osc} := 1/|\kappa_1|$ is the radius of the osculating sphere at \mathbf{x}_b . It follows that the quadratic form (B.1) is positive definite when either \mathbf{x}_0 is outside the ellipsoid, or the distance of \mathbf{x}_0 from inside is smaller than R_{osc} .

References

- [1] Barnett, A., Wu, B., and Veerapaneni, S. (2015). Spectrally accurate quadratures for evaluation of layer potentials close to the boundary for the 2D Stokes and Laplace equations. *SIAM Journal on Scientific Computing*, 37(4):B519–B542.
- [2] Beale, J. T. and Lai, M.-C. (2001). A method for computing nearly singular integrals. *SIAM Journal on Numerical Analysis*, 38(6):1902–1925.
- [3] Beale, J. T. and Tlupova, S. (2024). Extrapolated regularization of nearly singular integrals on surfaces. *Advances in Computational Mathematics*, 50(4):61.

- [4] Carvalho, C., Khatri, S., and Kim, A. D. (2018). Asymptotic analysis for close evaluation of layer potentials. *Journal of Computational Physics*, 355:327–341.
- [5] Chiu, S.-H., Moore, M. N. J., and Quaife, B. (2020). Viscous transport in eroding porous media. *Journal of Fluid Mechanics*, 893:A3.
- [6] Duan, R. and Rokhlin, V. (2009). High-order quadratures for the solution of scattering problems in two dimensions. *Journal of Computational Physics*, 228(6):2152–2174.
- [7] Gimbutas, Z. and Veerapaneni, S. (2013). A fast algorithm for spherical grid rotations and its application to singular quadrature. *SIAM J. Scientific Computing*, 35(6):A2738–A2751.
- [8] Helsing, J. (2013). A higher-order singularity subtraction technique for the discretization of singular integral operators on curved surfaces. *arXiv:1301.7276 [math]*. arXiv: 1301.7276.
- [9] Helsing, J. and Ojala, R. (2008). On the evaluation of layer potentials close to their sources. *Journal of Computational Physics*, 227(5):2899–2921.
- [10] Izzo, F., Runborg, O., and Tsai, R. (2022). Corrected trapezoidal rules for singular implicit boundary integrals. *Journal of Computational Physics*, 461:111193.
- [11] Khatri, S., Kim, A. D., Cortez, R., and Carvalho, C. (2020). Close evaluation of layer potentials in three dimensions. *Journal of computational physics*, 423:109798.
- [12] Klöckner, A., Barnett, A. H., Greengard, L., and O’Neil, M. (2013). Quadrature by expansion: A new method for the evaluation of layer potentials. *Journal of Computational Physics*, 252:332–349.
- [13] Kress, R. (2014). *Linear Integral Equations*, volume 82 of *Applied Mathematical Sciences*. Springer New York, 3 edition.
- [14] Morse, M. J., Rahimian, A., and Zorin, D. (2021). A robust solver for elliptic PDEs in 3D complex geometries. *Journal of Computational Physics*, 442:110511.
- [15] Nitsche, M. (2021). Evaluation of near-singular integrals with application to vortex sheet flow. *Theoretical and Computational Fluid Dynamics*, 35(5):581–608.
- [16] Nitsche, M. (2022). Corrected trapezoidal rule for near-singular integrals in axisymmetric stokes flow. *Advances in Computational Mathematics*, 48(5):57.
- [17] Nitsche, M., Oza, A. U., and Siegel, M. (2024). On the stability of an in-line formation of hydrodynamically interacting flapping plates.
- [18] Ockendon, H. and Ockendon, J. R. (1995). *Viscous Flow*. Cambridge Tests in Applied Mathematics. Cambridge University Press.

- [19] Pérez-Arancibia, C., Faria, L. M., and Turc, C. (2019). Harmonic density interpolation methods for high-order evaluation of laplace layer potentials in 2d and 3d. *Journal of Computational Physics*, 376:411–434.
- [20] Pozrikidis, C. (1992). *Boundary Integral and Singularity Methods for Linearized Viscous Flow*. Cambridge University Press.
- [21] Sidi, A. (2012). Euler–Maclaurin expansions for integrals with arbitrary algebraic endpoint singularities. *Mathematics of Computation*, 81(280):2159–2173.
- [22] Sohn, S.-I. (2024). Simulation of the unsteady vortical flow of freely falling plates (article). *Theoretical and Computational Fluid Dynamics*, 38(6):779–799.
- [23] Wu, B. (2024). An extension of the Euler-Maclaurin summation formula to nearly singular functions. *arXiv preprint arXiv:2409.19192*.
- [24] Wu, B. and Martinsson, P.-G. (2021a). Corrected trapezoidal rules for boundary integral equations in three dimensions. *Numerische Mathematik*, 149(4):1025–1071.
- [25] Wu, B. and Martinsson, P.-G. (2021b). Zeta correction: a new approach to constructing corrected trapezoidal quadrature rules for singular integral operators. *Advances in Computational Mathematics*, 47(3).
- [26] Wu, B. and Martinsson, P.-G. (2023). A unified trapezoidal quadrature method for singular and hypersingular boundary integral operators on curved surfaces. *SIAM Journal on Numerical Analysis*, 61(5):2182–2208.
- [27] Ying, L., Biros, G., and Zorin, D. (2006). A high-order 3d boundary integral equation solver for elliptic PDEs in smooth domains. *Journal of Computational Physics*, 219(1):247–275.
- [28] Zhu, H. and Veerapaneni, S. (2022). High-order close evaluation of laplace layer potentials: A differential geometric approach. *SIAM Journal on Scientific Computing*, 44(3):A1381–A1404.